Near Field millimeter Wave Antenna Measurements

Bharath Manjunatha
bh7472ma-s@student.lu.se

Department of Electrical and Information Technology
Lund University

Supervisor: Mats Gustafsson

Examiner: Daniel Sjöberg

November 4, 2023

Printed in Sweden
Tryckeriet i E-huset, Lund

Acknowledgement

I would like to express my sincere gratitude to Mats Gustafsson, my university supervisor from Lund University, for his expertise, mentorship, and valuable feedback that significantly contributed to the success of this thesis. I would like to express my gratitude to Daniel Sjöberg for accepting my request to be my thesis examiner. I would also like to thank Srinivas Dhoola, my thesis supervisor at Ericsson, for providing me with valuable insights, direction, and continuous support during this research endeavor. Furthermore, I extend my appreciation to Sofie Westerdahl, my manager at Ericsson, for her encouragement and support throughout the thesis project.

I am grateful to Lund University and Ericsson for providing me with the academic resources and environment necessary for pursuing my master's degree and conducting this research. I am also thankful to my family, friends, and all those who have supported me in various ways during this academic journey.

Abstract

In the real world, understanding an antenna's radiation pattern is crucial for its proper utilization. Typically, antennas are tested in the far-field region, where the radiation lobes are fully developed and phase errors are less than $\pi/8$. However, due to some drawbacks like an increase in far-field distance for antenna arrays, researchers have shifted towards near-field measurements. These near-field measurements are then used to implement algorithms that predict the antenna's radiation pattern in the far field. In this thesis, an algorithm is developed in MATLAB to predict the far-field pattern of a horn antenna and estimate its gain at frequencies of 28 GHz and 39 GHz. Additionally, probe compensation is implemented to eliminate the influence of the probe's radiation pattern. In this study, planar near-field measurement techniques have been employed to scan the radiation pattern, which comes with angle constraints. Additionally, an effort has been made to extend this approach to active antennas by utilizing a Phased Array Antenna Module (PAAM) board. However, due to time limitations, only an estimation of the gain of the PAAM board has been conducted. In the discussion of the results, potential reasons have been identified to justify any deviations from the expected results. Finally, future work has been proposed to enhance the implemented algorithm and achieve more accurate results.

Popular Science Summary

Understanding how antennas emit signals, even though they are invisible, is truly fascinating. But why is it important to know how antennas radiate signals? The answer is quite simple: if a user doesn't receive a signal properly, they won't have the best experience. Let's imagine someone is on a phone call; if they don't get a good signal, the conversation won't be clear. So, for everyday situations like this, knowing about antenna radiation patterns is crucial.

However, measuring these radiation patterns needs to be done from a considerable distance away from the antenna. The reason for this is that when you're very close to the antenna, the signal isn't as strong as you might think. Unfortunately, it works the other way around. If the observer is very close to the antenna, the user might be in what's called the "near-field" region, where the antenna's signal pattern isn't fully formed. Also, in real-life situations, users won't always be sitting right next to the antenna when they use it.

Obtaining the far-field pattern through near-field measurements might sound confusing, but it's actually possible and quite useful. The reason for using this method is that in newer cellular generations like 5G or 6G, larger antenna arrays are used at higher frequencies, which means the far-field distance increases due to larger antenna array size, making direct measurements very challenging. So, measuring it in the near field and then using these measurements to estimate the far-field pattern is much more convenient.

When you're transforming measurements from the near field to the far field, it's crucial to consider something called "probe compensation." But what exactly is a probe? Well, a probe is essentially another antenna used to measure the radiation of the antenna you're testing. Now, why do we need to compensate for the probe? That's because, just like the antenna being tested, the probe itself is also an antenna. It has its own radiation pattern, which can affect the measurements you take of the antenna under test. So, by doing probe compensation, we're essentially removing the impact of the probe's own radiation pattern from the data we've measured. This helps us get a more accurate picture of the antenna's performance.

By scanning in the near field, we can gain insights into antenna radiation. We can do these measurements on flat surfaces, curved surfaces like cylinders, or in spherical coordinates. Using this method has several advantages. It works well in small testing spaces, makes it easier to position antennas, helps detect near-field effects, and is cost-effective, among other benefits.

Table of Contents

List of Figures

List of Tables

Acronyms

3GPP	Third Generation Partnership Project
5G NR	Fifth Generation New Radio
AAS	Advanced Antenna Systems
DL	Down-Link
DUT	Device Under Test
EM	Electromagnetic
FF	far Field
FT	Fourier transform
GPIB	General Purpose Interface Bus
HFSS	High-Frequency Structure Simulator
I	Input
IF	Intermediate Frequency
LO	Local Oscillator
NF	Near-field
NF2FF	Near-field to Far-field
O	Output
OERWG	Open-Ended Rectangular Waveguide
OTA	Over the Air
PAAM	Phase Array Antenna Module
RF	Radio frequency
RNF	Radiating Near Field
Rx	Receiver
S	Scattering
SA	Spectrum Analyzer
Tx	Transmitter
UL	Up-Link
USB	Universal Serial Bus
VNA	Vector Network Analyzer

Chapter 1
Introduction

1.1 Motivation

In daily life, communication is the fundamental basis of sharing information across the globe. Despite the invention of wired communication (telephone) in 1876 [1], humans always seek comfort in their day-to-day activities as wired communication has disadvantages. For instance, it lacks mobility during usage, is difficult to install as it requires more time and resources, and can be challenging to troubleshoot in faulty situations [2]. In light of these drawbacks, researchers invented wireless communication technology in 1895 [3], which revolutionized the world's perspective on communication. This technology provided the freedom to transmit and receive data without cables or wires. The physical connections were replaced by electromagnetic signals broadcast, to transfer data between the transmitter and the receiver.

Antennas are fundamental to wireless communication systems [4]. They are responsible for changing Radio frequency (RF) signals on wires into electromagnetic waves. The transmitting antenna receives current at its input and subsequently emits energy as electromagnetic waves. Conversely, the receiving antenna captures the electromagnetic radiation and converts it into current, which is then amplified and processed in subsequent stages. A Tx/Rx antenna can be either a single antenna or an array of antennas with more features known as Advanced Antenna Systems (AAS). An array antenna can be used for beam steering which also provides higher gain and directivity compared to single antenna. A phased array antenna is one in which the radiation pattern of each individual element constructively combines with all other elements to form an effective radiation pattern, known as the main lobe [5].

In Fifth Generation New Radio (5G NR), AAS plays a vital role in achieving higher data rates, increased capacity, and various other advantages. Within the AAS framework, the size of antenna elements diminishes as frequencies rise, and a substantial number of antenna elements are employed in an array. This combination of reduced antenna element size and an expanded array size, along with the integration of radio chains into the antenna board, presents significant challenges for traditional measurement techniques that rely on connecting cables

or probes to the test boards. To address these challenges, the industry introduced Over the Air (OTA) measurements, which have been standardized to assess radio performance in wireless systems [6]. While measurements are typically conducted in the far-field, 3GPP has approved three different measurement methods: direct far-field, indirect far-field, and near-field measurements.

The radiation patterns, polarization, and gain of an antenna are ideally measured on the surface of a sphere with a constant radius. Any position on this sphere is known by the spherical coordinates. Since the radial distance is fixed, only θ and ϕ are sufficient to identify the position. The representation of the radial characteristics of an antenna as a function of θ and ϕ at a constant radial distance in the far field is known as the radiation pattern of an antenna [4]. This thesis focuses on the precise prediction of antenna radiation patterns.

1.2 Goal

The goal of this master thesis can be divided into the following sub-goals:

- To verify the functionality of planar measurement setup.
- Study and implement an algorithm in MATLAB capable of predicting the far-field pattern of an antenna based on the near-field measurements, including probe compensation.
- To propose a method for conducting near-field measurements for active antennas.
- To implement the proposed method for active antenna only if time and resource permit.

1.3 Challenges

As near-field measurements are not a direct measurement of the antenna radiation pattern, several challenges need to be addressed:

- Selecting the appropriate algorithm for the Near-field to Far-field (NF2FF) transformation is crucial as it is specific to the measurement setup and application.
- Hardware issues must be taken into consideration to ensure reliable and accurate measurements.
- The results, including the probe effects, are not ideal, which makes it imperative to choose an accurate probe compensation method.
- Proper alignment of the Device Under Test (DUT) and the near-field probe is essential for obtaining accurate results.
- During field transformation, higher precision is expected in measurements, including choosing the appropriate step size and considering mutual coupling effects due to distance and other factors.

- Ensuring accuracy concerning the far field is of utmost importance as this process involves predicting the far-field pattern and not directly measuring it.
- In the case of active antennas, maintaining phase synchronization between Local Oscillator (LO) and Intermediate Frequency (IF) signals is prioritized.

1.4 Outline

The structure of the next chapters of the report is as follows:

- Chapter 2 provides an overview of the fundamental concepts required for the project.
- Chapter 3 explains the design and methodology implemented in the project.
- Chapter 4 presents and explains the results of the project.
- Chapter 5 discusses future work and presents the conclusion of the project.

As this project is carried out in Ericsson, the report is published in two forms. The detailed version is confined to Ericsson alone, while an edited version is made available to everyone.

Chapter 2

Theoretical Background

A very useful property of an antenna is reciprocity, which states that the transmit and receive properties of an antenna are identical [4]. This means that if the radiation pattern of the transmit mode is known, it is the same as that of the receiving mode. The radiation pattern of an antenna can be obtained from either the near field or the far field. Obtaining it from the far field is most suitable for small antennas and can also be performed outdoors as the far field distance is relatively close. However, for large and high frequency antennas, obtaining the radiation pattern from the far field becomes a tedious process [7]. Hence, it is suggested to utilize the near field radiation to predict the far field radiation pattern of such antennas.

2.1 Field Regions

The space around the antenna is divided into three regions [4]:

- **Reactive Near-field:** The region is defined as "that portion of the near-field region immediately surrounding the antenna wherein the reactive field predominates [4]." The outer boundary of this region is approximated by $0.62\sqrt{D^3/\lambda}$, starting from the surface of the antenna. Here, D is the largest dimension of the antenna, and λ is the wavelength.

- **Radiating Near-field (Fresnel):** The region is defined as "that region of the field of an antenna between the reactive near-field region and the far-field region wherein radiation fields predominate and wherein the angular field distribution is dependent upon the distance from the antenna. For an antenna focused at infinity, the radiating near-field region is sometimes referred to as the Fresnel region on the basis of analogy to optical terminology [4]."

  This region will not exist if the maximum dimension of an antenna is much smaller than the wavelength. This region extend from the outer surface of the reactive near field region to a distance less than $2D^2/\lambda$. Since this region is far enough from the antenna, it doesn't contain a reactive component, so back-coupling of the fields becomes out of phase. Thus, it cannot return

inductive or capacitive energy from antenna currents [4]. Hence, this region is utilized for NF2FF transformation.

- **Far-field (Fraunhofer):** The region is defined as "that region of the field of an antenna where the angular field distribution is essentially independent of the distance from the antenna [4]." This region starts from a distance of $2D^2/\lambda$, extending up to infinity. The pattern in the reactive near field is more spread, mostly uniform. As it is moved towards the radiating near field, it is seen that the pattern forms lobes. Finally, in the far-field region, the patterns are well defined with one major lobe and several minor lobes, as shown in Figure 2.1.

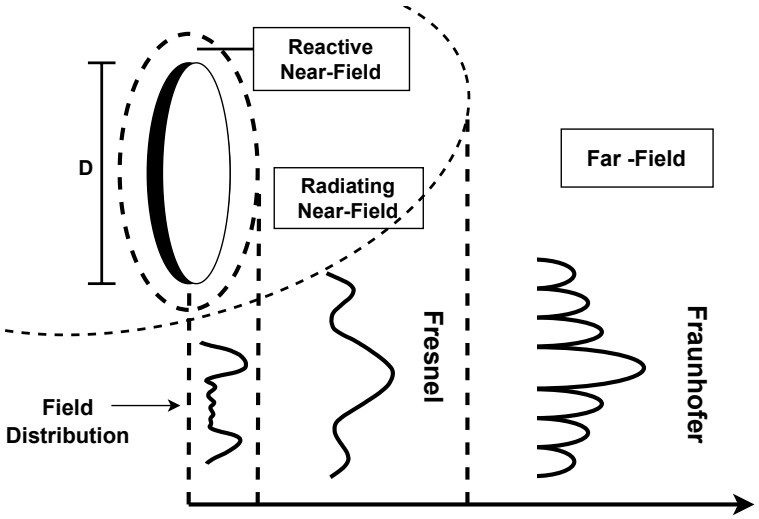

Figure 2.1: Field Distribution of an antenna: Reactive near-field very close to antenna, reactive field dominates, Fresnel region is between reactive NF and FF and Fraunhofer region is the FF region of antenna. [4]

2.1.1 Comparison of Near-field and Far-field

Near-field antenna measurements offer several advantages that make them an attractive choice for testing antennas in various applications [8]. The reduced testing space requirement allows for the use of smaller anechoic chambers, resulting in cost savings and greater practicality, especially in situations with limited space. The higher accuracy at close distances allows for detailed characterization of the antenna's performance near the radiating element. Additionally, the flexibility in antenna placement provides ease in testing antennas with non-standard configurations or those mounted on complex structures. However, near-field measurements come with some challenges [9]. They often require a longer test range or time to achieve comparable accuracy to far-field measurements, making them potentially more time-consuming. Additionally, the complex probe calibration process

demands meticulous attention to detail. Accurate measurements are crucial for near-to-far field transformations, and any errors or inaccuracies during the measurement process can impact the quality of the transformed far-field radiation pattern.

Far-field antenna measurements, on the other hand, present several advantages that have established them as a widely-used and standardized testing method [4]. Their accurate far-field characterization provides comprehensive insights into the antenna's radiation pattern, particularly in regions where the antenna operates most frequently. Far-field measurements follow standardized test methods, ensuring consistency. Despite these advantages, there are also challenges associated with far-field measurements. The setup cost for large anechoic chambers can be high, making it a considerable investment. In outdoor environments, there is a risk of reflection errors affecting the accuracy of measurements, especially when multi-path effects come into play. Properly addressing these challenges is essential for obtaining reliable and meaningful results from far-field antenna measurements.

2.2 Plane waves

A plane wave is an idealized electromagnetic wavefront characterized by uniform amplitudes and phase across its perpendicular planes [10]. This concept simplifies the description of the propagation of electromagnetic waves through free space, allowing us to model their behavior accurately. The uniform plane wave and its properties are very important as the superposition of plane waves represents a complicated wave type. This is because, a uniform plane wave is the simplest type of electromagnetic wave [11]. For the near-field measurements, understanding plane waves is crucial because the transition from the near-field to the far-field occurs when the electromagnetic wavefront resembles a plane wave at a certain distance from the antenna. As a result, the characteristics of the radiating antenna in the near-field region can provide valuable insights into the antenna's far-field performance.

The near-field measurements conducted are integral to capturing the complex spatial distribution of electromagnetic fields in the immediate vicinity of the antenna. By acquiring this detailed information, it is possible to extrapolate and manipulate the data to derive far-field patterns. However, to achieve accurate far-field predictions, it is required to employ algorithms that leverage the principles of plane wave propagation. These algorithms utilize the near-field data to approximate the antenna's radiation characteristics in the far-field, where the electromagnetic wavefront assumes a plane wave-like structure. Thus, a comprehensive understanding of plane waves ensures the validity and reliability of the algorithm for far-field prediction.

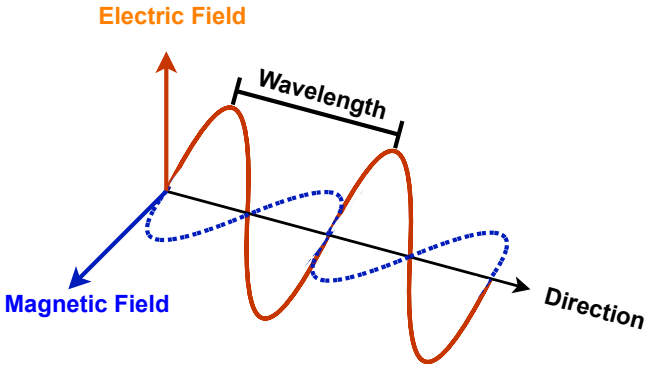

Figure 2.2: Electromagnetic Plane Wave

Considering a uniform wave plane with amplitude E_0 and propagating in z direction with electric and magnetic field in x and y direction respectively. It's given by the following equations:

$$E = E_0 \cos(\omega t - kz)\hat{x} = Re\left[\tilde{E}e^{j\omega t}\right] \tag{2.1}$$

$$\tilde{E} = \hat{x}E_0 e^{-jkz} \tag{2.2}$$

$$\tilde{H} = \hat{y}\frac{E_0 e^{-jkz}}{\eta_0} \tag{2.3}$$

$$H = Re\left[\tilde{H}e^{j\omega t}\right] \tag{2.4}$$

where, η_0 is the intrinsic impedance of free space.

2.3 Field using Potentials

To simplify the analysis, it is common to introduce auxiliary functions known as vector potentials. The two vector potentials are the magnetic vector potential and the electric vector potential [4]. Utilizing the potentials often simplifies the process of obtaining $\bar{E}$ and $\bar{H}$, even though it may require determining additional functions like electric vector potential denoted by $\bar{V}$ and magnetic vector potential denoted by $\bar{A}$ as shown in Figure 2.3.

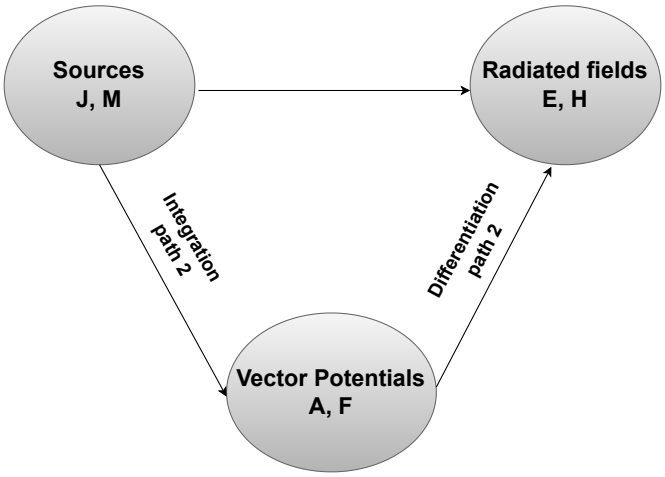

Figure 2.3: Block diagram for computing fields radiated by electric and magnetic sources [4]

In the near-field technique, a planar surface at distance h from DUT is meshed into $L_x \times L_y$ cells, so the tangential fields are measured at the center of each cell(i,j) as shown in Figure 2.4. The electric and magnetic fields of an antenna can be found using vector potentials. These fields are described by the following equations [12]:

$$\bar{M_{ij}} = -\hat{n} \times \bar{E}_{ij} \tag{2.5}$$

$$\bar{J_{ij}} = \hat{n} \times \bar{H}_{ij} \tag{2.6}$$

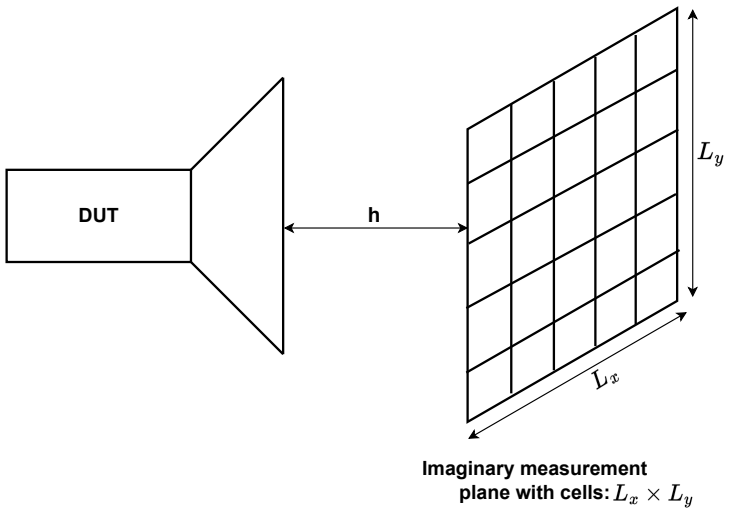

Figure 2.4: Representation of measurement plane with $L_x \times L_y$ cells

With equivalent currents, the vector potentials $\bar{V}$ and $\bar{A}$ are first calculated, using which $\bar{E}$ and $\bar{H}$ are calculated. R_{ij} is the distance from any point on the source to the observation point.

$$\bar{V_{ij}} = \frac{\epsilon}{4\pi} \int \bar{M_{ij}} \frac{e^{-j\beta R_{ij}}}{R_{ij}} dS' \tag{2.7}$$

$$\bar{A_{ij}} = \frac{\mu}{4\pi} \int \bar{J_{ij}} \frac{e^{-j\beta R_{ij}}}{R_{ij}} dS' \tag{2.8}$$

$$\bar{E} = \sum \sum [-\frac{1}{\epsilon} \bigtriangledown \times \bar{F_{ij}} - j\omega \bar{A_{ij}} - j\frac{1}{\omega\mu\epsilon} \bigtriangledown (\bigtriangledown \cdot \bar{A_{ij}})] \tag{2.9}$$

$$\bar{H} = \sum \sum [-j\omega \bar{F_{ij}} - j\frac{1}{\omega\mu\epsilon} \bigtriangledown (\bigtriangledown \cdot \bar{F_{ij}}) + \frac{1}{\mu} \bigtriangledown \times \bar{A_{ij}}] \tag{2.10}$$

Initially, this method was adopted, but a major problem that arose with this approach was numerical errors. Calculating the numerical curl of the potential required more sophisticated algorithms, which were not implemented, resulting in increased noise and a subsequently high level of error.

Chapter 3

Design and Implementation

The initial trial of the Near-field to Far-field (NF2FF) transformation technique was introduced in the 1950s [12]. Firstly, complete electromagnetic field configurations surrounding an antenna were measured. These fields were utilized to form the equivalent source and determine the far field pattern using the Huygens-Fresnel principle [13]. As the Huygens principle requires a closed surface, planar, cylindrical, and spherical wave functions were introduced to carry out the model expansion and estimate the far-field radiation [14].

3.1 Methodology

This section outlines the sequential procedures followed for this thesis:

- Study: Conducted an in-depth literature review to establish a theoretical foundation.
- Scanner verification and error correction: Assessed the existing antenna scanner's code and hardware for functionality. Identified and rectified errors to ensure proper operation.
- Measurements: Performed electromagnetic field measurements using the verified and error-corrected scanner.
- Probe Correction: Applied meticulous probe correction to ensure accurate near-field data.
- NF2FF Transformation: Utilized the NF2FF technique to derive far-field radiation patterns.
- Verification: Validated predicted far-field patterns against existing data and theoretical expectations.

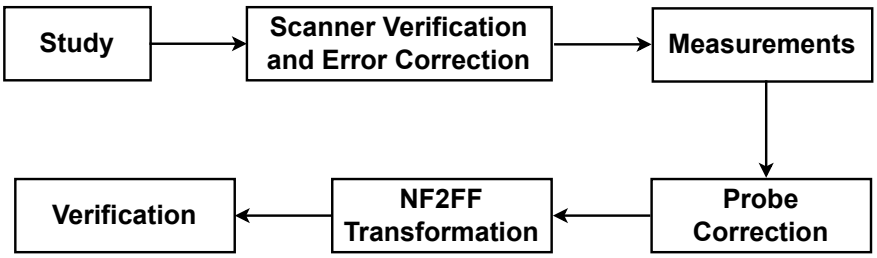

Figure 3.1: Block diagram depicting the procedures followed

3.2 Antenna Under Test

3.2.1 Passive Antenna

A passive antenna is a basic, non-amplified device that does not require any external power source for its operation. It relies solely on the properties of its physical design to transmit or receive electromagnetic waves [15]. These waves are radiated outward into the surrounding space, carrying the same frequency as the input signal.

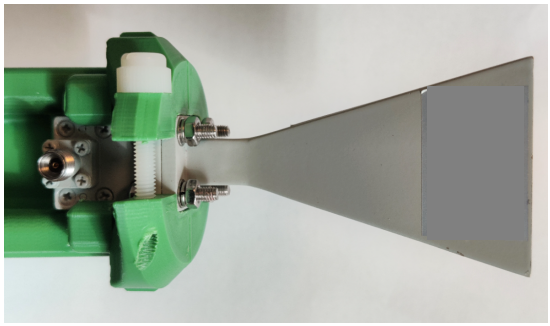

Figure 3.2: Photo of the used horn antenna

A single source horn antenna provided by the company is used as the DUT, as they are among the simplest antennas, often exhibiting a directional radiation pattern with high antenna gain. The gain of horn antennas typically increases (and the beam width decreases) as the frequency of operation is increased [4]. The antenna's specifications used in the project are stated in Table 3.1.

Parameters	Value
Frequency (GHz)	26.5 - 40
Wave guide Type	WR28
Gain (dBi)	20
Polarization	Linear
Size (mm)	32.1 x 40.4 x 94
Material	Copper

Table 3.1: Specifications of the Horn Antenna in Figure 3.2

3.2.2 Active Antenna

An active antenna with input LO and IF signals utilize built-in active components, such as amplifiers and signal processors, powered by an external source. This integration enables the antenna to convert and radiate signals at the desired radio frequency on the transmitter side and vice versa on the receiving side [15]. The integration of active components allows active antennas to boost the received signal and enhance their transmitting capabilities.

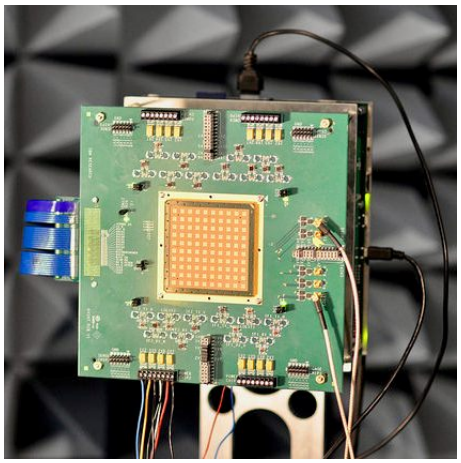

Figure 3.3: Photo of the used PAAM Board [16]

The Phase Array Antenna Module (PAAM) board utilized in the project is designed for Fifth Generation New Radio (5G NR) purposes. It is equipped with an antenna array at the front end, operating in the frequency band n257 (Local multi-point distribution service). According to Third Generation Partnership Project (3GPP) standards, this frequency band ranges from 26.50 GHz to 29.50 GHz, for both Up-Link (UL) and Down-Link (DL) [17]. The board is designed to offer high gain and withstand extreme temperature conditions.

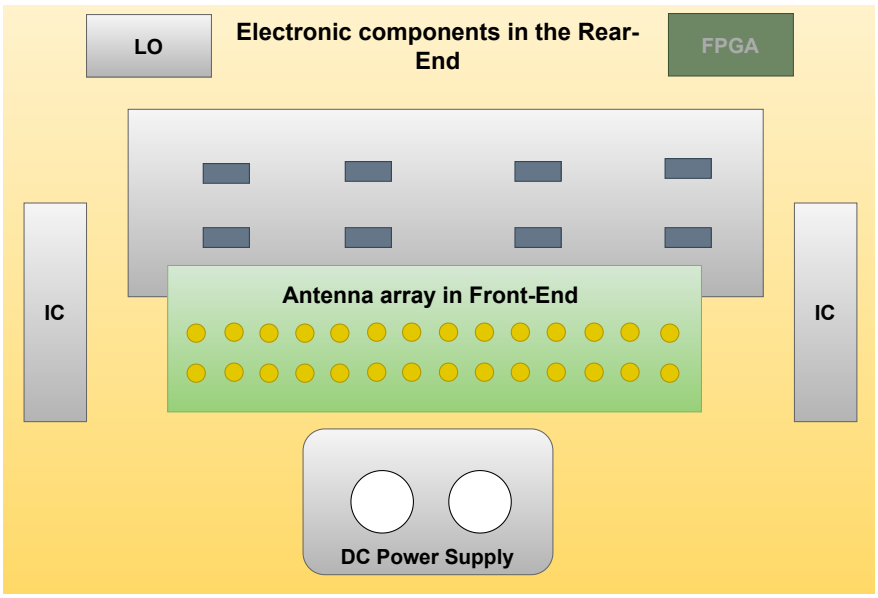

Figure 3.4: Block diagram of the used PAAM Board

3.3 Probe

3.3.1 Probe 1

Near-field measurements are based on utilizing near-field probes, which collect the electric field, magnetic field, or a combination of both at a particular point in space. The Open-Ended Rectangular Waveguide (OERWG) is one of the most commonly used probes in near-field measurements, especially in planar and cylindrical systems [18]. The influence of geometrical parameters on the measurements is studied for both the horn antenna and the OERWG. The results clearly demonstrate that the OERWG probe provides higher and more accurate measured fields compared to the horn antenna, especially for predicting the far-field pattern of the DUT. This experiment and its results are presented in [18].

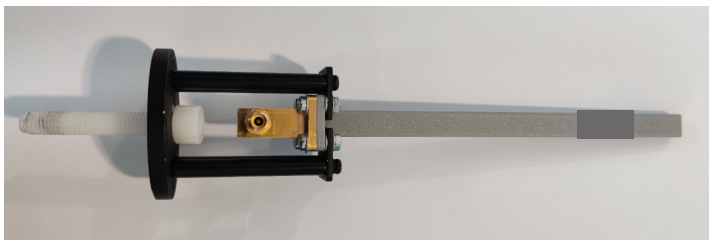

Figure 3.5: Open-Ended Rectangular Waveguide Probe with coaxial adapter

Moreover, the OERWG probe's unique rectangular waveguide shape allows for straightforward integration into planar measurement setups. This design feature makes it highly suitable for scanning across the planar surface of the DUT, capturing near-field data with ease and precision.

The OERWG probe used in the thesis is the same as the one employed in previous work on a similar topic. Consequently, the simulation data are already known and extracted from the earlier research. For further details, the complete work can be referred to in [19]. The technical specifications of the probe are listed in Table 3.2.

Parameters	**Value**
Frequency (GHz)	26.5 - 40
Wave guide Type	WR28
Connector (mm)	2.92 female
Size (mm)	7.1 x 3.5 x 150
Material	Copper

Table 3.2: Specifications of the Probe 1

Based on the probe specifications, the simulation model of the probe was designed using the Ansys HFSS tool to cover the frequency range from 26 GHz to 42 GHz. This was achieved by varying the length of the waveguide from 100 mm to 250 mm. The gain of the waveguide concerning different lengths and frequencies is presented in Figure 3.6. It is evident that there is an increase in gain as the frequency rises, while the change in length has a very negligible or no effect on the gain of the probe.

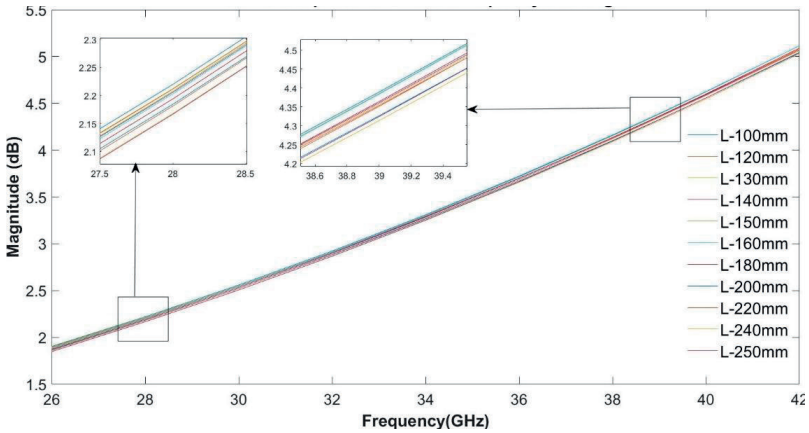

Figure 3.6: Gain of the probe for different frequencies and lengths [19]

Figure 3.7 depicts the S11 parameter of the probe for various frequencies and

probe lengths. The results indicate that the magnitude of S11 decreases as the frequency increases, with a maximum difference of 0.3 dB due to the variation in length. However, an unexpected error occurring at approximately 30 GHz is not a concern for this project, as it could be attributed to a software sampling error.

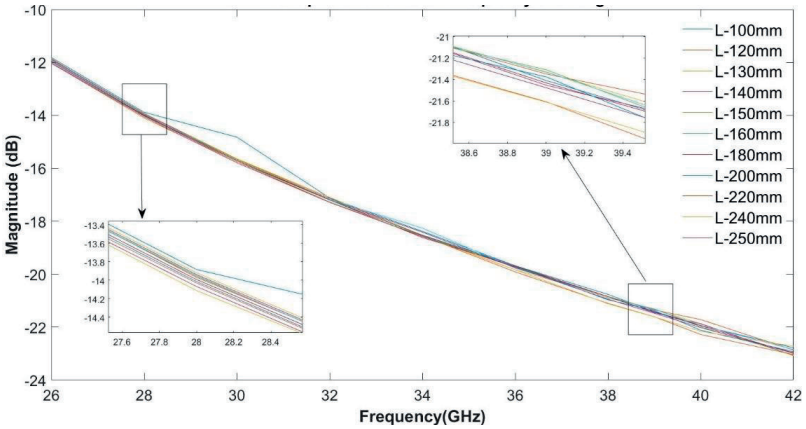

Figure 3.7: S11 of the probe for different frequencies and lengths [19]

3.3.2 Probe 2

To compare the results with the measurements obtained using a different probe, a similar OERWG probe is chosen with different dimensions, and its gain and directivity are provided by the manufacturer. The details of the probe are as shown in the Table 3.3.

Parameters	**Value**
Frequency (GHz)	26.5 - 40
Waveguide Band	WR28
Polarisation	Linear
Dimensions (mm) (L x W x H x D)	311 x 406 x 406 x 280
Material	Copper
Gain (dBi) at 28GHz	5.89
Efficiency (dB) at 28GHz	-0.80
Return Loss (dB) at 28GHz	-11.97

Table 3.3: Specifications of the Probe 2

3.4 Scanner

The near-field data, typically comprising amplitude and phase measurements, is acquired by scanning the antenna using a near-field probe over a predefined surface, which can be planar, cylindrical, or spherical. Subsequently, the measured data is transformed into the far-field pattern.

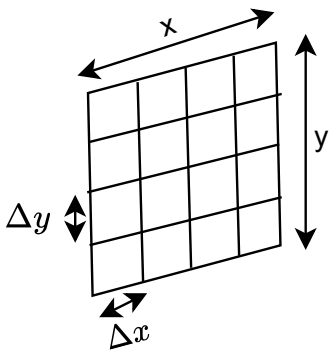

Planar Scanning:
In general, planar measurements are conducted for high-gain antennas. This technique requires minimal computations and does not involve any movement of the DUT. The acquisition of planar near-field data is usually performed over a rectangular x-y grid, as shown in Figure 3.8. The maximum sampling space for the near field should be equal to $\Delta x = \Delta y = \lambda/2$ [4].

Figure 3.8: Planar Scanning [4]

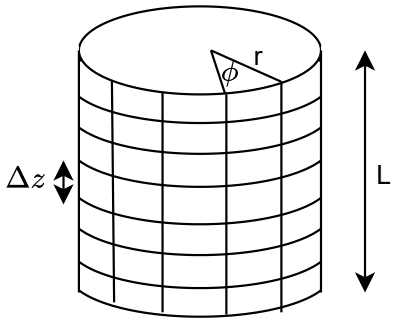

Cylindrical Scanning:
In this scanning technique, the DUT is mounted on a motor that rotates in the ϕ direction, while the probe moves around the cylindrical surface with varying Δz to conduct the near-field measurements. Although the cylindrical system requires more computations than the planar approach, for many antennas, its measuring, positioning, and probe equipment are the least expensive options [4].

Figure 3.9: Cylindrical Scanning [4]

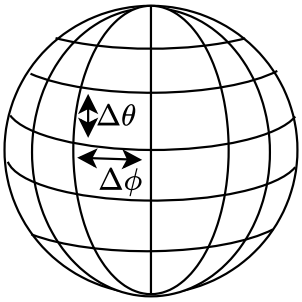

Spherical Scanning:
The spherical system requires the most expensive setup and antenna/probe positioning equipment, making it particularly significant for large antennas. This system is best suited for measurements of low gain and omni-directional antennas [4].

Figure 3.10: Spherical Scanning [4]

In this scanning technique, the DUT is mounted on a motor that rotates in the ϕ direction, while the probe moves around the cylindrical surface with varying Δz to conduct the near-field measurements. Although the cylindrical system requires more computations than the planar approach, for many antennas, its measuring, positioning, and probe equipment are the least expensive options.

3.4.1 Designed Scanner

In the project, planar near-field scanning is used. As mentioned in Section 3.1, the existing scanner at the company was chosen to reduce time and cost. However, it was later verified and altered as required due to errors in the code's design. The planar scanner was chosen as it was easier to implement and data processing is simpler. The scanner moves in the x-y direction with the maximum scan area of 165 mm $\times$ 175 mm. The scanner is as shown in Figure 3.11.

The movement of the scanner is achieved using a stepper motor. The NEMA 17 stepper motor is employed for building this scanner, featuring a rated voltage of 5 V, holding torque of 49 N/cm, a step angle of 1.8 degrees, and 200 steps per revolution [19]. From the GUI, it is determined that the maximum steps in the x-direction are 1674, and in the y-direction are 1818. Consequently, the resolution of the stepper motor is calculated to be 10.1454 steps/mm in the x-direction and 10.3886 steps/mm in the y-direction.

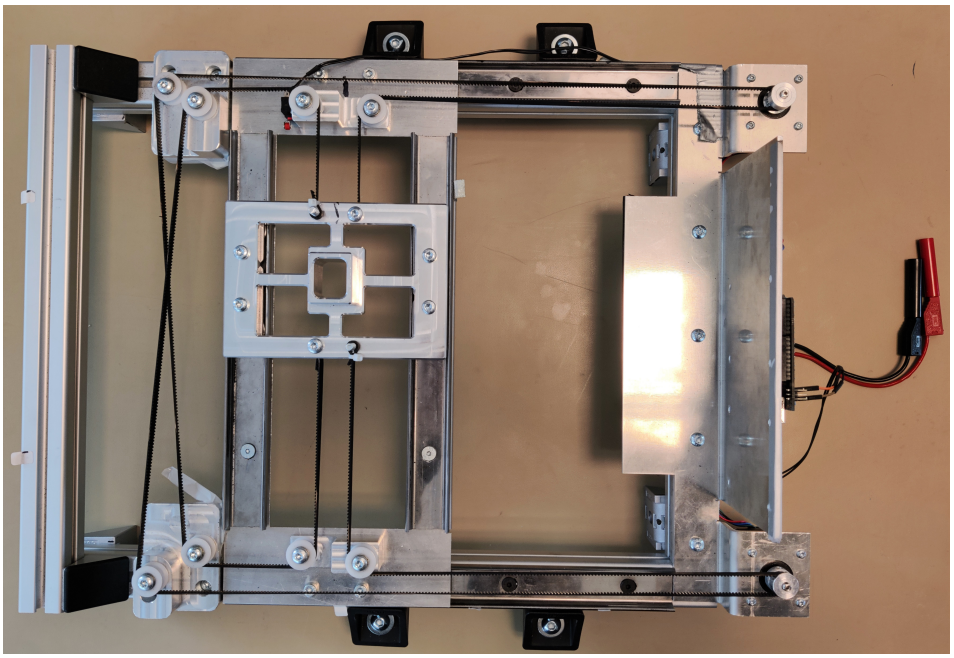

Figure 3.11: Photo of the designed scanner on which the probe will be fixed to move in the XY plane for conducting measurements.

To control the movement of the stepper motor in the required steps and direction, an Arduino Uno microcontroller board based on the ATmega328P is used. However, to provide enough current for the stepper motor to rotate, an external module called Adafruit motor shield is utilized. This is because the Arduino itself cannot supply sufficient current through its Input (I) - Output (O) pins to drive the stepper motor. As the stepper motor requires a stepper controller, the Adafruit motor shield is employed to energize the phases in a timely sequence to make the motor run.

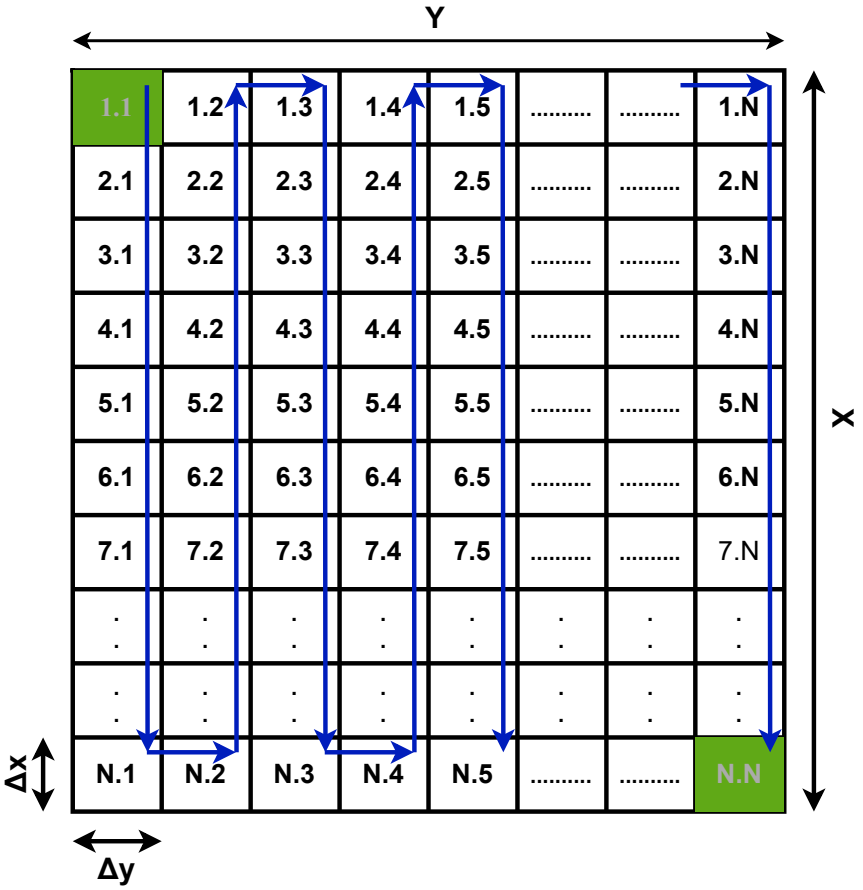

Figure 3.12: Movement Pattern of the Scanner

The scanner requires 1674 × 1818 motor steps to cover the entire scan area of 165 mm × 175 mm. Code was developed in Arduino IDE to control steps, speed and direction which was later uploaded to Arduino. An interface was built to control the scan area based on required step size using python. The movement of the scanner is depicted in Figure 3.12. Depending on the step size, the matrix can be selected in such a way that the scan area doesn't exceed 165 mm × 175 mm.

3.4.2 Distance and Sampling

The distance between the DUT and the probe during near-field measurements is crucial. The chosen distance for the measurements depends on several factors, as follows:

- The distance selected should be within the range of the radiating near-field zone, as mentioned in Section 2.1.
- A minimum separation of $3\lambda - 5\lambda$ is required to avoid evanescent modes

contributing to the measured near-field data. This is because determining the probe response at these modes is challenging.

- The valid region of the predicted radiation pattern decreases for a given scan area if the distance increases within the radiating near-field region. This is because the angular distribution depends on the distance between the DUT and the probe.

- However, choosing a very close distance to increase the valid angular range may result in errors in the measured data. This is because as the distance decreases, multiple reflections between the DUT and the probe increase, which may lead to mutual coupling.

Based on the dimensions of the antenna and the formula mentioned in Section 2.1. the distance are calculated for different frequencies and mentioned in Table 3.4.

Frequency (GHz)	**Near-field (mm)**	**Far-field(mm)**	**Valid Separation Distance (mm)**
28	48	305	$48 \leq$ RNF $<$ 305
39	57.7	429.5	$57.7 \leq$ RNF $<$ 429.5

Table 3.4: Valid Separation Distance between DUT and Probe

The sampling points on the measuring grid are chosen in such a way that they do not exceed $\lambda/2$ to satisfy the Nyquist sampling criteria, i.e., $\Delta x = \Delta y \leq \lambda/2$. The scan area must be sufficiently large to capture all the radiation from the antenna. In other words, the larger the scan area, the more data would be captured, leading to a higher valid angle. Otherwise, the angular range through which the predicted far field is valid is given by Equation 3.1 [19].

$$\theta_{\pm} = \arctan\left(\frac{L_{\pm} - \frac{D}{2}}{z}\right) \tag{3.1}$$

where,
$L_{\pm}$ represents the length of the portion of the scan above or below the z-axis.
D is the diameter of the DUT.
z is the separation distance between the DUT and the probe.

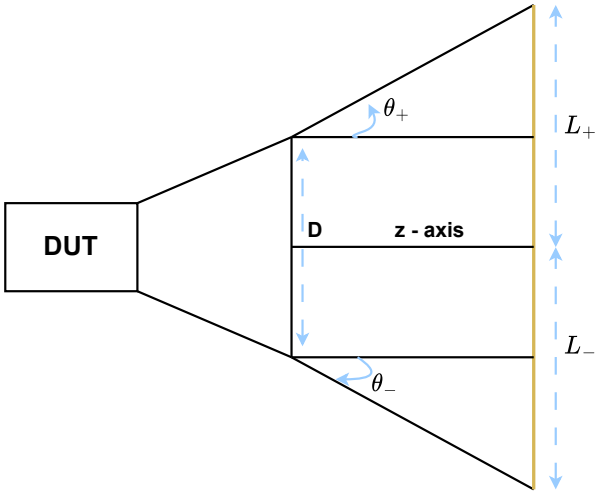

Figure 3.13: Scan Plane

After evaluating Equation 3.1, the valid angular range is determined for the total scan length of 165 mm at different frequencies and various valid separation distances. The results are presented in Table 3.5.

Frequency (GHz)	Distance (mm)	Valid angle (degree)
28	48 (minimum)	52.38
	300 (maximum)	11.73
39	57.7 (minimum)	47.19
	425 (maximum)	8.33

Table 3.5: Valid Angular Range

3.5 Near Field Data

The anechoic chamber, utilized for conducting near field planar measurements, has dimensions approximately 68 cm × 73 cm × 165 cm. The inner walls of the chamber are completely shielded using radio wave absorbers, typically in cone-shaped forms. These absorbers prevent signal reflections from the surfaces, ensuring that the antenna's radiation can be accurately measured without any interference.

The planar near field measurements require several components, including an Arduino, Vector Network Analyzer (VNA), power supply, GPIB USB Bus interface, a computer, and RF cables. The VNA serves as a signal generator on the Tx side, while also measuring the signal received at the probe end. The RF cables must be calibrated using the standard E-cal, and the GPIB USB bus interface is utilized to connect the VNA to the system. The measurement setup is as shown in the Figure 3.14.

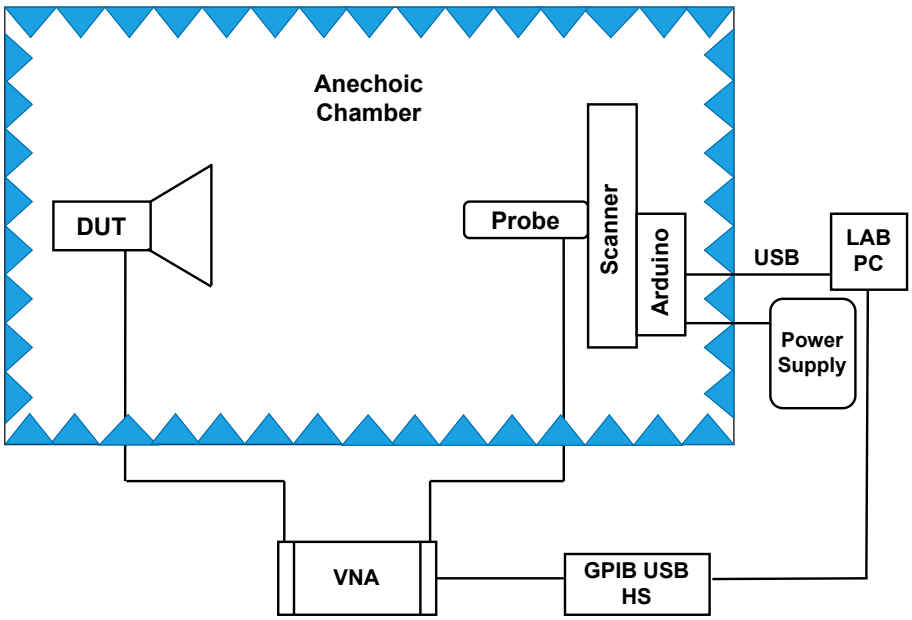

Figure 3.14: Representation of the measurement setup in the project: the DUT and the probe mounted on the scanner, which is controlled by a programmed Arduino is placed inside an anechoic chamber. Both the DUT and the probe are connected to VNA, which, in turn, is connected to a laboratory PC. Additionally, the Arduino is powered by an external power supply.

Vector Network Analyzer: The VNA is an instrument used to measure network parameters. It is capable of measuring both the transmitted and reflected scattering of signals. The Scattering (S) parameters are preferred for these measurements, especially at higher frequencies, due to their ease of measurement. The measured S parameters include both the amplitude and phase of the signals.

GPIB: GPIB instruments offer test and manufacturing engineers the widest selection of vendors and instruments for general-purpose to specialized vertical market test applications. It is one of the most common interfaces used to transfer data between instruments. The National Instruments GPIB-USB-HS is used in this project to communicate with the VNA using a computer.

```
Moving to start position (1,1): (685,1110)

---------------------------------------------------------------------

Choose:
Manual measurements, press m
Automatically run all measurements, press a
Exit, press e
:a

Automatic probing Started
---------------------------------------------------------------------

10:42:01 --> Saved results for coordinates:(1,1) --> steps (685,1110)
10:42:04 --> Saved results for coordinates:(2,1) --> steps (837,1110)
10:42:07 --> Saved results for coordinates:(3,1) --> steps (989,1110)
10:42:10 --> Saved results for coordinates:(3,2) --> steps (989,954)
10:42:13 --> Saved results for coordinates:(2,2) --> steps (837,954)
10:42:16 --> Saved results for coordinates:(1,2) --> steps (685,954)
10:42:19 --> Saved results for coordinates:(1,3) --> steps (685,798)
10:42:22 --> Saved results for coordinates:(2,3) --> steps (837,798)
10:42:25 --> Saved results for coordinates:(3,3) --> steps (989,798)
---------------------------------------------------------------------

Result is stored in file: Chamber_Probing_2023-01-02_10_39.csv
Test setup is stored in file: Chamber_Probing_2023-01-02_10_39.txt

---------------------------------------------------------------------

Step motors: Power off

Done !!
```

Figure 3.15: Measurement and storage of result

The DUT and probe are aligned so that their coordinates are parallel. The probe is mounted on the scanner, and the scanning area is adjusted according to the step size and scan length. The amplitude and phase of the S parameters are measured and stored in an Excel sheet on the local storage of the computer as shown in the Figure 3.15.

3.6 Near Field to Far Field Transformation

Horn antenna in Figure 3.2 is a type of aperture antenna. An aperture is defined as "A surface, near or on an antenna, on which it is convenient to make assumptions regarding the field values for the purpose of computing fields at external points [20]. The aperture is often taken as that portion of a plane surface near the antenna, perpendicular to the direction of maximum radiation, through which the major part of the radiation passes [20]." The radiation from an antenna is induced by the current present either on the surface or on the aperture of the antenna [21]. To analyze the far field pattern, it is beneficial to decompose the entire current on the antenna surface into small current elements (see Figure 3.16). By doing this, the total radiation field can be treated as the sum of the radiated fields from each of these small current elements present on the surface of the antenna. This approach simplifies the computation of the antenna's far-field radiation pattern, which mainly depends on the distance from the antenna.

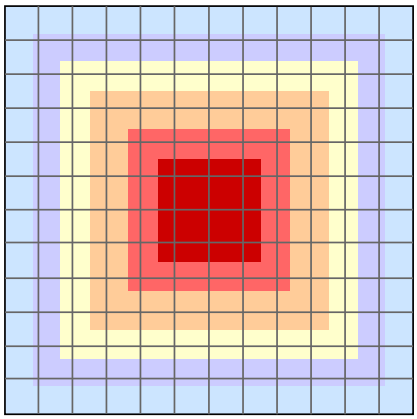

Figure 3.16: Current elements on the surface of horn antenna

The phase of the signals cannot be neglected to know the accurate radiation fields of an antenna. It is known that Electromagnetic (EM) waves propagates at speed of light c_0. So, to propagate a distance d, it takes time $T = d/c_0$. Here time harmonic signals are considered, so there will be delays when a signal is reached to the receiver by each current element. The time delay, in frequency domain corresponds to a phase shift, i.e., the Fourier transform (FT) of a time delay [21].

$$F(\omega) = \int e^{-j\omega t} f(t)\, dt \Rightarrow \int e^{-j\omega t} f(t-T)\, dt \tag{3.2}$$

$$F_T(\omega) = \int e^{-j\omega\left(t'+T\right)} f(t')\, dt' \tag{3.3}$$

$$F_T(\omega) = e^{-j\omega T} F(\omega) \tag{3.4}$$

Equation 3.4 shows that it is equivalent to taking the original Fourier Transform and multiplying it by a phase factor. In some cases, certain current elements might be closer to the receiver, requiring phase compensation for those signals. This phase compensation is accomplished by the introduced phase factor in Equation 3.4. The phase factor in Equation 3.4 can be simplified as $e^{-j\omega T} = e^{-j\omega d/c_0} = e^{-jkd}$, where k represents the wave number [21].

Each current element on the surface of the antenna should be treated with its own phase. This is necessary because the interference at the receiver may vary depending on whether it is in-phase or out-of-phase, resulting in either constructive or destructive interference. Figure 3.17 illustrates this concept with two current elements.

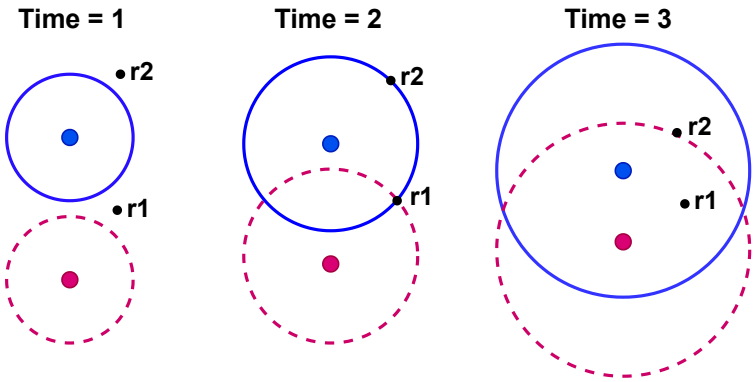

Figure 3.17: Interference at the receiver [21]

3.6.1 Current to far-field interpretation

The distance to every current element on the aperture is essential, and not just the center of the surface. When considering a single current element r' and an observer at a distance r, the equations from 3.5 to 3.8 can be derived using Taylor expansion. This concept is closely related to the sampling points mentioned in Section 3.4.2. During measurements, it is assumed that the sampling points are chosen in a way that ensures the current is constant between the sampling points.

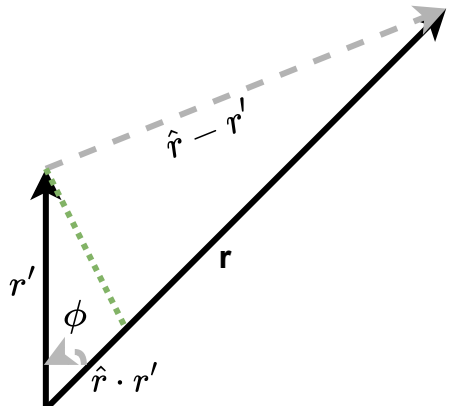

Figure 3.18: r represents the distance between a single current element r' and an observer at a distance r, with ϕ denoting the angle between them.

$$|r - r'| = \sqrt{(r - r') \cdot (r - r')} = \sqrt{r^2 - 2rr' + |r'|^2} \tag{3.5}$$

$$|r - r'| = r\sqrt{1 - 2\hat{r} \cdot r'/r + |r'|^2 / r^2} \approx r\sqrt{1 - 2\hat{r} \cdot r'/r} \tag{3.6}$$

$$|r - r'| \approx r(1 - \hat{r} \cdot r'/r) = r - \hat{r} \cdot r' \tag{3.7}$$

$$|r - r'| \approx r - |r'| \cos\phi \tag{3.8}$$

As the current element r' is much smaller compared to the receiver distance r, Equation 3.8 is derived. This result arises from the fact that the observer's distance is significantly large, allowing us to treat the distance to all the current elements on the antenna surface as approximately the same, unless the antenna is tilted at a specific angle. Now, the time delay transforms into a phase factor in the frequency domain. In other words, the time delay experienced by the signals is represented as a phase shift.

$$e^{-jk|r-r'|} \approx e^{-jk(r-\hat{r}\cdot r')} = e^{-jkr} e^{jk\hat{r}\cdot r'} \tag{3.9}$$

In Equation 3.9, the approximation is made under the assumption that the observer or receiver is in the far field of the antenna. The resulting equation consists of two terms. The first term e^{-jkr} depends on the coordinates and the observation point, indicating how the radiation wavefront propagates to the observer. On the other hand, the second term $e^{jk\hat{r}\cdot r'}$ depends on the source and the direction of the observer in the far zone. Notably, this term does not rely on the distance between the observer or receiver and the source [21]. The fields on the surface or aperture of an antenna can be represented by equivalent currents. Specifically, both surface electric and magnetic currents are present [22]. The surface electric current is generated by the surface magnetic field, while the surface magnetic current is induced by the surface electric field. When applying the cross product with the $\hat{n}$ component, the vector undergoes a 90-degree rotation, leading to the emergence of these surface currents.

$$J = \hat{n} \times H \tag{3.10}$$

$$J_m = -\hat{n} \times E \tag{3.11}$$

Therefore the far field vector of an antenna from the current density is given by Equation 3.12 and 3.13.

$$F(\theta, \phi) = F(\hat{r}) = \int J(r') e^{jk\hat{r}\cdot r'} dS' \tag{3.12}$$

$$F_m(\theta, \phi) = F_m(\hat{r}) = \int J_m(r') e^{jk\hat{r}\cdot r'} dS' \tag{3.13}$$

Here, F depends on $\hat{r}$, represented by the spherical coordinates θ and ϕ. The antenna follows the right-hand rule, implying that in the far field, the electric field, magnetic field, and direction of propagation ($\hat{r}$) are all mutually perpendicular. Furthermore, far away from the sources in the far field region, the field can be locally approximated as plane waves propagating in the $\hat{r}$ direction. Moreover, the solution of Maxwell's equations using the vector potential shows that $E \sim \hat{r} \times (F \times \hat{r})$. As a result of these factors, the radial component is eliminated from the far-field vector.

Since the aperture of the horn antenna is planar, we can simplify Equations 3.12 and 3.13. Considering that the aperture lies in the xy-plane, we can express dS' as $dx'dy'$. As a result, the radiation vectors are reduced to:

$$F(\theta,\phi) = \int_A J(x',y')e^{j(k_x x' + k_y y')}dx'dy' \tag{3.14}$$

$$F_m(\theta,\phi) = \int_A J_m(x',y')e^{j(k_x x' + k_y y')}dx'dy' \tag{3.15}$$

where, $k_x = k\cos\phi\sin\theta$, $k_y = k\sin\phi\sin\theta$ and $k = 2\pi/\lambda$

As described in Section 3.4.2, the sampling points are deliberately chosen to maintain a constant current between these points. This allows us to approximate the integration as a summation over the entire aperture region. Consequently, we can simplify Equations 3.14 and 3.15 to:

$$\begin{aligned} a &= p\Delta x \\ b &= q\Delta y \end{aligned} \tag{3.16}$$

$$F(\theta,\phi) = \sum_{p=1}^{N}\sum_{q=1}^{N} J(p,q)e^{j(k_x a + k_y b)}\Delta x\Delta y \tag{3.17}$$

$$F(\theta,\phi) = \sum_{p=1}^{N}\sum_{q=1}^{N} (J_x(p,q)\hat{x} + J_y(p,q)\hat{y})e^{j(k_x a + k_y b)}\Delta x\Delta y \tag{3.18}$$

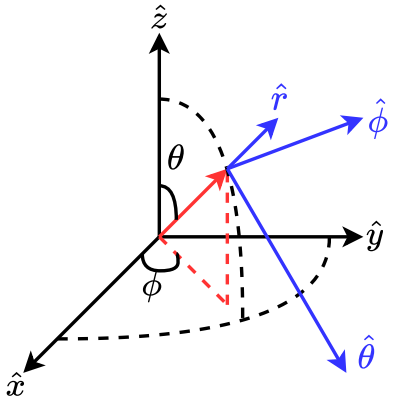

A spherical coordinate system (r,θ,ϕ) has the unit vectors,

$$\hat{x} = \hat{r}\sin\theta\cos\phi + \hat{\theta}\cos\theta\cos\phi - \hat{\phi}\sin\phi$$
$$\hat{y} = \hat{r}\sin\theta\sin\phi + \hat{\theta}\cos\theta\sin\phi + \hat{\phi}\cos\phi$$
$$\hat{z} = \hat{r}\cos\theta - \hat{\theta}\sin\theta$$

that defines a local coordinate system with unit vectors,

- $\hat{r}$ in the direction of increasing r.
- $\hat{\theta}$ in the direction of increasing θ.
- $\hat{\phi}$ in the direction of increasing ϕ.

Figure 3.19: Spherical Coordinate system

$$F(\theta,\phi)=\sum_{p=1}^{N}\sum_{q=1}^{N}(J_{xpq}(\hat{\theta}\cos\theta\cos\phi-\hat{\phi}\sin\phi)+J_{ypq}(\hat{\theta}\cos\theta\sin\phi+\hat{\phi}\cos\phi))e^{j(k_xa+k_yb)}\Delta x\Delta y \tag{3.19}$$

The relation between rectangular and spherical coordinates can be used by eliminating the radial component in Equation 3.18. Henceforth, $J(p,q)$ will be represented as J_{pq} to simplify the representation. Equation 3.19 represents the far-field pattern of an antenna. Here, $F(\theta)$ and $F(\phi)$ can be determined separately, indicating the pattern variation in the directions of $\hat{\theta}$ and $\hat{\phi}$, respectively [21].

$$F(\theta)=\left(\sum_{p=1}^{N}\sum_{q=1}^{N}\left(J_{x(pq)}\cos\theta\cos\phi+J_{y(pq)}\cos\theta\sin\phi\right)\left(e^{j(k_xa+k_yb)}\right)\Delta x\Delta y\right)\hat{\theta} \tag{3.20}$$

$$F(\phi)=\left(\sum_{p=1}^{N}\sum_{q=1}^{N}\left(J_{x(pq)}\cos\phi-J_{y(pq)}\sin\phi\right)\left(e^{j(k_xa+k_yb)}\right)\Delta x\Delta y\right)\hat{\phi} \tag{3.21}$$

The far-field electric radiation pattern of an antenna, which varies in the $\hat{\theta}$ and $\hat{\phi}$ directions, can be predicted using the near-field data with Equations 3.20 and 3.21, respectively. To predict the far-field magnetic radiation pattern of an antenna, the electric current should be replaced by the magnetic current. The explanation for the magnetic field is similar to that for Equations 3.20 and 3.21. The magnetic far-field is represented by Equations 3.22 and 3.23.

$$F_m(\theta)=\left(\sum_{p=1}^{N}\sum_{q=1}^{N}\left(J_{m(x(pq))}\cos\theta\cos\phi+J_{m(y(pq))}\cos\theta\sin\phi\right)\left(e^{j(k_xa+k_yb)}\right)\Delta x\Delta y\right)\hat{\theta} \tag{3.22}$$

$$F_m(\phi)=\left(\sum_{p=1}^{N}\sum_{q=1}^{N}\left(J_{m(x(pq))}\cos\phi-J_{m(y(pq))}\sin\phi\right)\left(e^{j(k_xa+k_yb)}\right)\Delta x\Delta y\right)\hat{\phi} \tag{3.23}$$

3.7 Probe Compensation

The orientation of the probe with respect to the test antenna changes as the vertical location of the probe changes. Thus, probe correction is usually required in planar cases [4]. The principle behind probe compensation is to account for the effects of the measurement probe on the measured fields. The probe introduces changes in the amplitude and phase of the fields, and these changes need to be corrected to obtain an accurate representation of the DUT's radiation properties. Practical probes are not ideal, so to get accurate results, some sort of probe compensation technique should be used [8] [23].

3.7.1 Kerns Transmission Equation - Generalized Method

Without considering the polarization issue for now, the coupling of antennas in the near field is described by the presented formulas. This is outlined using a simple scalar field, denoted as $u(r)$.

$$u(r) = a_0 \sum_{n=1}^{N} t_n u_n(r) \tag{3.24}$$

The field of the DUT is expanded into a complex set of modes, denoted as $u_r(r)$, with a_0 as the excitation. In practical terms, probes do not measure the field at a point in space, especially in near-field regions where significant variations in the fields may be observed over the volume of the probe [24]. To consider the influence of the probe, it's important to note how the probe responds to each mode in the expansion in equation 3.24:

$$w'_n(r', R') = [Pu_n](r', R') \tag{3.25}$$

Thus, the probe's response to the fields in equation 3.24 can be approximated as the superposition of its response to the contributing modes:

$$\frac{w'(r, R)}{a_0} = \sum_{n=1}^{N} w'_n(r, R) t_n \tag{3.26}$$

The modal expansion corresponding to the equation 3.24 with $k_x = \alpha$, $k_y = \beta$ and $k_z = \gamma$ is given by :

$$E(r) = \frac{a_0}{2\pi} \int_{-\infty}^{+\infty} \int_{-\infty}^{+\infty} t_0(\hat{k}) exp(ik \cdot r) \frac{d\alpha d\beta}{\gamma k}, z > z_0 \tag{3.27}$$

The response of the probe to each mode corresponding to the equation 3.25 is given by:

$$w'_{\alpha\beta}(r') = s'_\pi(\hat{k}) \cdot t_0(\hat{k}) exp(ik \cdot r') \tag{3.28}$$

Finally, corresponding to the equation 3.26, the Kerns transmission formula is shown in equation 3.29. This approximation is valid when multiple reflections can be ignored and when the probe and the DUT can be physically separated by a plane perpendicular to $\hat{z}$.

$$\frac{w'(r)}{a_0} = \int_{-\infty}^{+\infty} \int_{-\infty}^{+\infty} s'_\pi(\hat{k}) \cdot t_0(\hat{k}) exp(ik \cdot r) \frac{d\alpha d\beta}{\gamma k} \tag{3.29}$$

The Fourier transforms in equation 3.29 may be inverted to yield,

$$\begin{aligned} T'_{\alpha\beta} &= s'_\pi(\hat{k}) \cdot t_0(\hat{k}) = s^{1'}_{\alpha\beta} e^1(\hat{k}) + s^{2'}_{\alpha\beta} e^2(\hat{k}) \\ T'_{\alpha\beta} &= \frac{\gamma k}{4\pi^2} \int_{-\infty}^{+\infty} \int_{-\infty}^{+\infty} \frac{w'(r)}{a_0} exp(-ik \cdot r) dx dy, z = d \end{aligned} \tag{3.30}$$

with equations,

$$\begin{aligned} t_0(\hat{k}) &= t^1_{\alpha\beta} e^1(\hat{k}) + t^2_{\alpha\beta} e^2(\hat{k}) \\ s'_\pi(\hat{k}) &= s^{1'}_{\alpha\beta} e^1(\hat{k}) + s^{2'}_{\alpha\beta} e^2(\hat{k}) \end{aligned} \tag{3.31}$$

Equation 3.30 provides one equation for the two unknown components of $t_0(\hat{k})$ since $T'_{\alpha\beta}$ can be computed from the data $w'(r)/a_0$ measured on the plane $z = d$. Data from the second probe are needed to provide sufficient information to solve $t_0(\hat{k})$.

$$\begin{pmatrix} T'_{\alpha\beta} \\ T''_{\alpha\beta} \end{pmatrix} = \begin{pmatrix} s^{1'}_{\alpha\beta} & -s^{2'}_{\alpha\beta} \\ s^{1''}_{\alpha\beta} & -s^{2''}_{\alpha\beta} \end{pmatrix} \begin{pmatrix} t^{1}_{\alpha\beta} \\ t^{2}_{\alpha\beta} \end{pmatrix} \tag{3.32}$$

$$\begin{pmatrix} t^{1}_{\alpha\beta} \\ t^{2}_{\alpha\beta} \end{pmatrix} = \frac{-i}{\hat{k} \cdot (s'_\pi \times s''_\pi)} \begin{pmatrix} -s^{2''}_{\alpha\beta} & s^{2'}_{\alpha\beta} \\ -s^{1''}_{\alpha\beta} & s^{1'}_{\alpha\beta} \end{pmatrix} \begin{pmatrix} T'_{\alpha\beta} \\ T''_{\alpha\beta} \end{pmatrix} \tag{3.33}$$

With two probes, the system can be represented as a linear system and the quantities associated with the second probe are marked with a double prime. The probe should be selected such that $s'_\pi(\hat{k}) \times s''_\pi(\hat{k}) \neq 0$. If the probe is linearly polarized, the second probe can be realized by rotating the same probe by 90° about its z-axis. The method is explained in detail in [24].

3.7.2 Pattern Subtraction Method- Implemented

As the far-field pattern of the DUT is estimated using the algorithm presented in section 3.6, it should be noted that the estimated pattern is influenced by the probe's characteristics. To account for this probe effect, the probe is designed and simulated according to the specifications outlined in section 3.3. Figures 3.20 and 3.21 depict the E-plane and H-plane of the probe at 28 GHz and 39 GHz respectively.

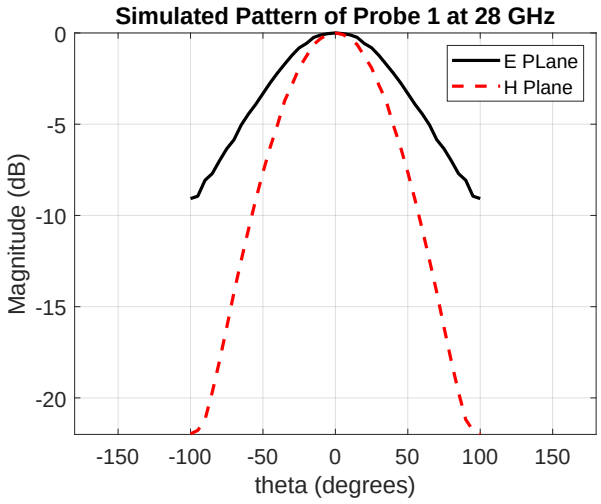

Figure 3.20: Simulated Probe 1 Pattern at 28GHz

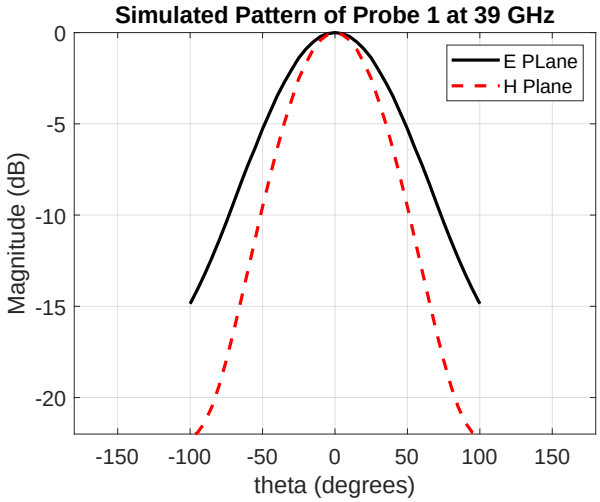

Figure 3.21: Simulated Probe 1 Pattern at 39GHz

Now that the magnitude of the probe at each angle is known, it is subtracted from the DUT's far-field pattern magnitude for the respective angle. With all magnitudes in dB, the compensated fields can be represented as follows:

$$Eplane_{pc}(\theta) = Eplane_{dut}(\theta) - Eplane_{sp}(\theta) \tag{3.34}$$

$$Hplane_{pc}(\theta) = Hplane_{dut}(\theta) - Hplane_{sp}(\theta) \tag{3.35}$$

where,
pc = Probe Compensated
dut = Estimated Pattern of DUT
sp = Simulated probe pattern

The reasons for deviating from the Kerns transmission method presented in section 3.7.1 to the implemented method were as follows:

- The standard probe compensation technique was recommended for application to the measured data. However, since this aspect of the thesis was not conducted within the company, raw measured data was unavailable for probe compensation. While the pattern subtraction method had an impact on the processed data.
- Time limitations required choosing a simpler method.
- Additionally, implementing this method offered an opportunity to investigate a technique and derive conclusions regarding its suitability for probe compensation.

3.8 Active Antenna: (PAAM)

While the NF2FF algorithm for active antennas remains consistent, the measurement technique requires careful consideration. When using a VNA, measuring the magnitude is relatively straightforward. However, precise phase measurements require special attention. Initially, phase calibration of the PAAM board is performed to ensure that it radiates at 0 degrees. It is performed by assigning weights to each antenna element relative to the center antenna element. While this calibration may not have a significant impact in the near-field region, where radiation is not yet fully developed, it proves valuable for validation after estimating the far-field results.

During the measurements, the probe records the amplitude at a specific point and calculates the phase in degrees choosing the phase of the center antenna element as reference.

The results obtained by following this algorithm for the measured NF data are presented and plotted, and their accuracy is discussed in Chapter 4 of the report.

Chapter 4
Results

This chapter presents the results of the project obtained from the design and implementation proposed in Chapter 3.

4.1 Setup and Estimated result of Passive Antenna: Horn

The measurement setup is depicted in Figure 4.1. The RF cables were carefully selected to align with the project's designated frequency range. Calibration was conducted through the utilization of the Ecal kit. Details pertaining to the reflection coefficients of both the DUT (S11) and the probe (S22) can be found in Table 4.1.

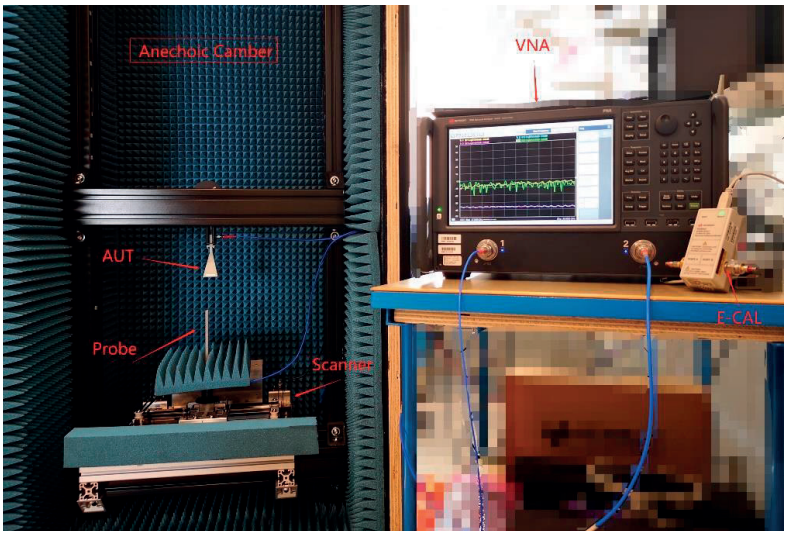

Figure 4.1: Measurement setup at Lab: The DUT, and probe fixed on the scanner with programmed arduino is in the anechoic chamber while both connected to VNA

Frequency (GHz)	DUT S11 (dB)	Probe S22 (dB)
28	-19.32	-11.56
39	-27.45	-15.4

Table 4.1: Reflection Coefficient values of DUT and Probe

The radiation patterns and gain of the DUT, employed within the project, are illustrated in Figure 4.2, 4.3 and Table 4.2 respectively. The radiation patterns and gain at both 28 GHz and 39 GHz adhere to the manufacturer-provided data. The polarization of the antenna corresponds to the direction of maximum radiation called E-plane. To explain further, if the antenna is horizontally polarized, the E-plane curve represents the strength of the electric field as it varies with observation angles. In contrast, the H-plane is perpendicular to the E-plane and represents the strength of the magnetic field in the vertical direction as it varies with angles in the θ direction. The concept of spherical angles is graphically depicted in Figure 3.19. The proposed NF2FF methodology, in Chapter 3, is expected to yield a radiation pattern and gain prediction that closely resembles that presented in Figure 4.2, 4.3 and Table 4.2 respectively.

Frequency (GHz)	Gain (dBi)
28	19.18
39	21.23

Table 4.2: Gain According to the manufacturer data sheet

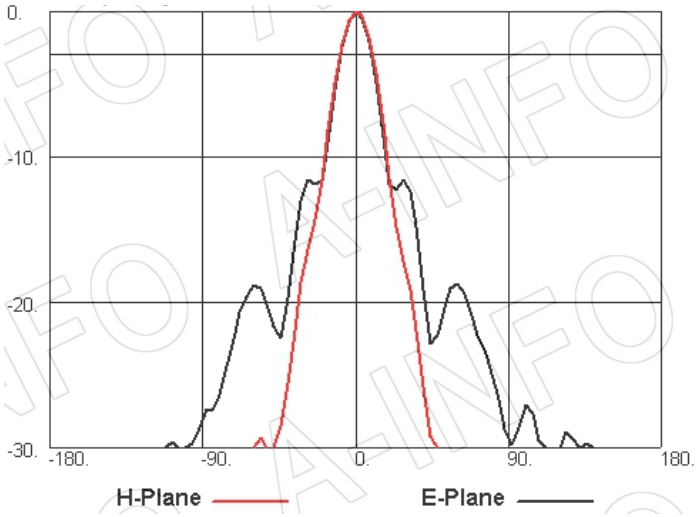

Figure 4.2: Radiation Pattern from the horn antenna Manufacturer at 28 GHz

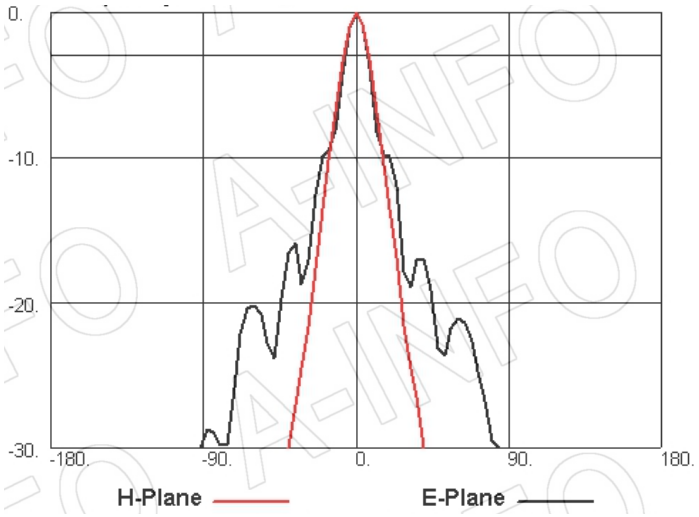

Figure 4.3: Radiation Pattern from the horn antenna Manufacturer at 39 GHz

4.2 Results for 28 GHz

The measurement setup for 28 GHz frequency is done with following parameters:

- Frequency, f = 28 GHz
- Wavelength, $\lambda = \frac{c}{f} = \frac{3\times10^8}{28\times10^9} = 0.0107$ m
- DUT diameter, D = 40.4 mm
- Radiating near field range according to Table 3.4 is, 48 mm $\leq$ RNF $\leq$ 305 mm

In this section, the estimated radiation pattern of the DUT is plotted while varying the distance and input power. The maximum scanned area achieved for a step size of 2 mm was 162 mm $\times$ 162 mm. This resulted in the collection of 6561 data points in a matrix of size 81×81 within the measurement setup. Subsequently, MATLAB script available on mathworks web page [25] is used to process these data points. Later, the NF2FF algorithm was implemented to predict the far-field pattern. The estimated radiation pattern is valid for certain angles $\theta_{\pm}$, which depend on the distance between the DUT and the probe. The validity of these angles has been verified through the obtained results. It is worth noting that the range of valid angles is inversely proportional to the separation distance.

One of the most crucial parameters of an antenna is its gain. The gain of an antenna in a specific direction is defined as "the ratio of the intensity, in a given direction, to the radiation intensity that would be obtained if the power accepted by the antenna were radiated isotropically. The radiation intensity corresponding

to the isotropically radiated power is equal to the power accepted (input) by the antenna divided by 4π" [4]. The horn antenna's gain at 28 GHz was indicated as 19.18 dBi in the manufacturer's datasheet. Gain estimation can be carried out using equations 4.2. The gain estimated from the obtained far-field pattern is 18.69 dBi. The datasheet provides a direct measurement of the far-field pattern, and the simulation closely resembles ideal cases with minimal errors. In this project, the far-field estimation is conducted, followed by gain calculation, which will experience measurement errors, losses, and approximation. These factors contribute to a slight difference of 0.49 dBi from the actual gain.

$$Gain = 4\pi \frac{\text{radiation intensity}}{\text{total input (accepted) power}} \tag{4.1}$$

$$Gain = 4\pi \frac{U(\theta, \phi)}{P_{\text{in}}} \tag{4.2}$$

The estimated radiation pattern in the Figure 4.4, to a reasonable extent, align with the patterns depicted in Figures 4.2. A slight gap is observed between the Eplane and Hplane, potentially accounting for the measurement errors. This disparity may arise due to a few factors. Firstly, certain sections of the chamber were left uncovered by absorbers, leading to reflections and signal scattering from the DUT. Additionally, reflections originating from the metallic structure of the scanner might contribute to this phenomenon. Another plausible explanation pertains to probe compensation. Despite the implementation of probe compensation, there exist alternative robust algorithms that could potentially yield more accurate outcomes. The outcomes of additional adjustments in distance and power are illustrated in Appendix A.

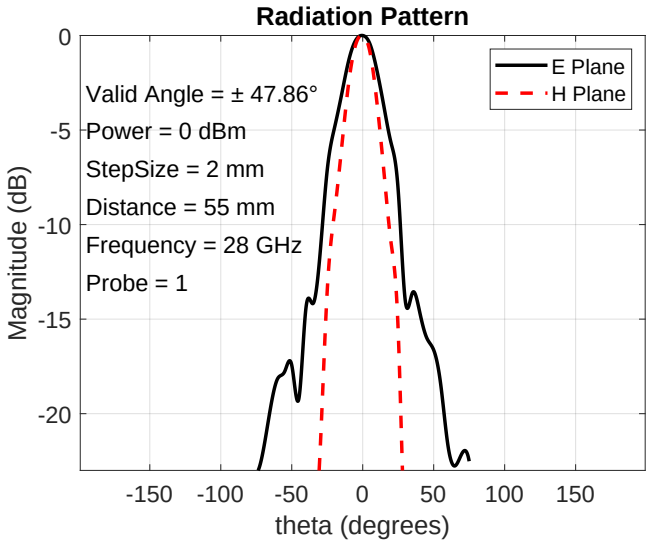

Figure 4.4: Estimated Pattern at 28 GHz with separation distance 55 mm

4.2.1 Comparison of the results

Using Probe 2 mentioned in section 3.3.2:
For result comparison, measurements were taken utilizing probe 2, as outlined in Section 3.3.2, at a separation distance of 55 mm and an input power of +10 dBm. The achieved result employing probe 2 for these measurements is depicted in Figure 4.5. Upon analysis, it is notable that the first side lobe of E plane peaks experience more loss than expected, but align with estimated pattern using probe 1. This occurrence might have been mitigated by employing a more robust algorithm for probe compensation. As for the H-plane, there is a high degree of similarity as both graphs coincide very well. This indicates that estimation from the different probes yields a similar pattern within an acceptable range.

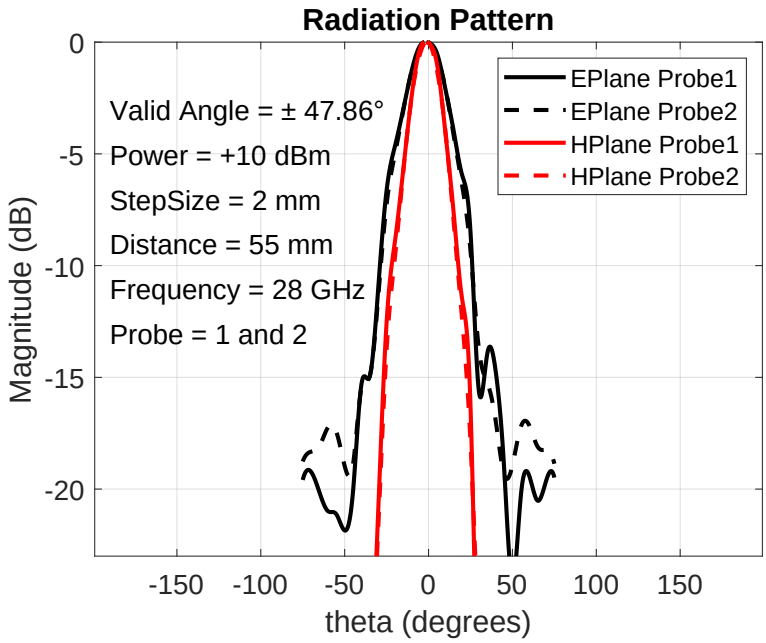

Figure 4.5: Comparison of estimated Pattern using probe 1 and 2

Varying Separation distance between DUT and probe:
Figure 4.6 depicts the graphs of the E-plane and H-plane patterns as the separation distance between the DUT and the probe varies. Upon analysis, it becomes evident that the estimated far-field pattern depends on the separation distance during measurement i.e., as the measurement distance increases, the estimated far-field pattern's valid angular range decreases. It is observed that a shorter separation distance yields results that closely align with the pattern in the figure 4.2, while an increase in separation distance leads to a loss of information about the estimated pattern.

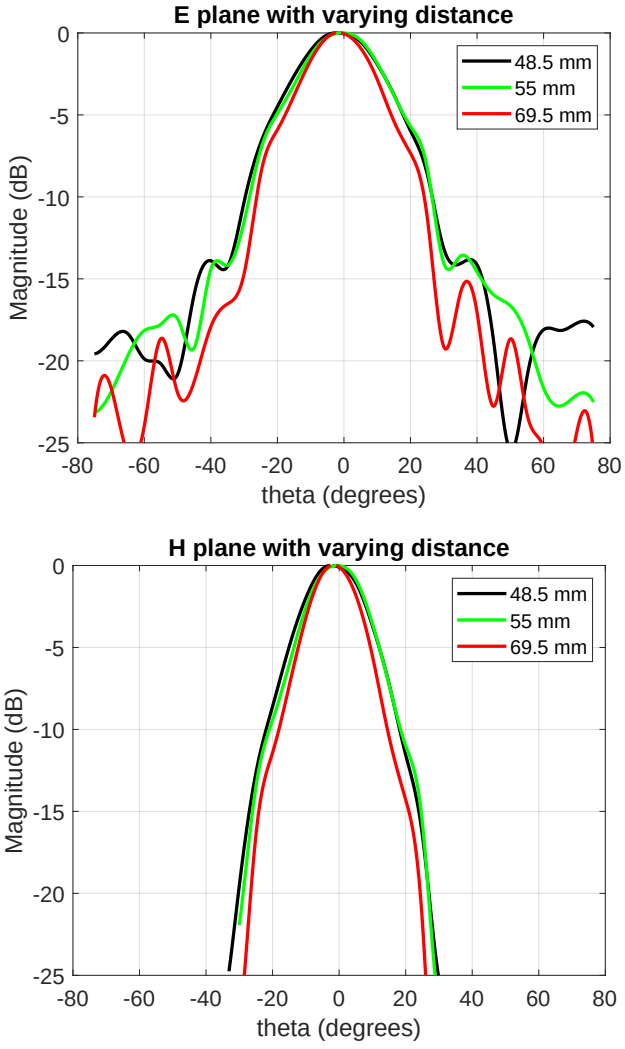

Figure 4.6: Estimated pattern for varying distance for 0 dBm input power at 28 GHz

Varying input power to the DUT:
Figure 4.7 illustrates the estimated pattern as we vary the input power to the DUT. The near-field measurements do not depend on the input power to the DUT. As expected, the variation in input power has minimal to no effect on the estimated pattern. This outcome can be attributed to the fact that the estimated pattern from near-field measurements is contingent on the measurement distance.

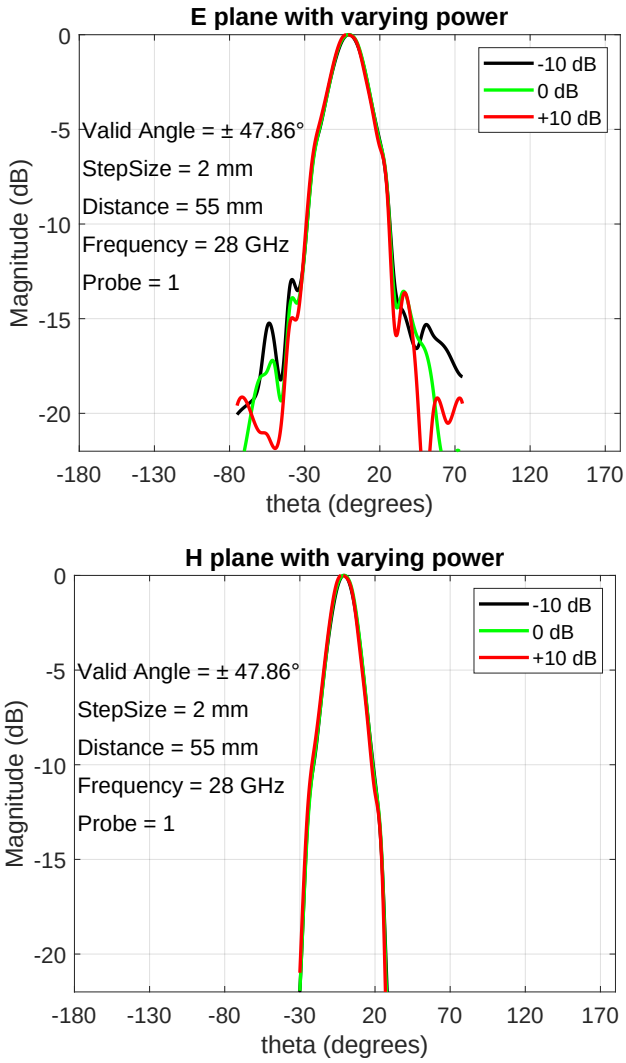

Figure 4.7: Estimated pattern for varying power to DUT with separation distance 55 mm at 28 GHz

4.3 Results for 39 GHz

The measurement setup for 39 GHz frequency is done with following parameters:

- Frequency, f = 39 GHz
- Wavelength, $\lambda = \frac{c}{f} = \frac{3\times10^8}{39\times10^9} = 0.0076$ m
- DUT diameter, D = 40.4 mm
- Radiating near field range according to Table 3.4 is, 57.7 mm $\leq$ RNF $\leq$ 429.5 mm

In this section, the estimated radiation pattern of the DUT is plotted while varying the distance. The maximum scanned area achieved for a step size of 1 mm was 163 mm $\times$ 163 mm. This resulted in the collection of 26,569 data points in a matrix of size 163×163 within the measurement setup. Subsequently, the NF2FF algorithm was implemented to process these data points. The estimated radiation pattern is valid for certain angles $\theta_{\pm}$, which depend on the distance between the DUT and the probe. The validity of these angles has been verified through the obtained results. It is worth noting that the range of valid angles is inversely proportional to the separation distance.

Referring to the gain parameter detailed in Section 4.2, the horn antenna's gain at 39 GHz is specified as 21.23 dBi in the antenna's datasheet. However, the gain calculated from the estimated radiation pattern in this project yielded 20.95 dBi. The explanation for the difference in gain remains consistent with that outlined in Section 4.2. Notably, given the higher frequency of 39 GHz compared to 28 GHz, the potential for errors is more pronounced, yet the handling of these challenges is effectively addressed.

The estimated results reasonably align with the patterns depicted in Figure 4.3, to a certain extent. A slight gap is observed between the Eplane and Hplane, potentially accounting for the measurement errors. This disparity may arise due to a few factors. Firstly, certain sections of the chamber were left uncovered by absorbers, leading to reflections and signal scattering from the DUT, which explains the higher disturbance in the estimated pattern. This effect is more pronounced at 39 GHz, as the wavelength is much shorter compared to 28 GHz, making it more susceptible to disturbances. Additionally, reflections originating from the metallic structure of the scanner might contribute to this phenomenon. Another plausible explanation pertains to probe compensation. Despite the implementation of probe compensation, there are alternative robust algorithms that could potentially yield more accurate outcomes.

The Figure 4.8, illustrate the estimated radiation pattern of DUT at 39 GHz while separation distance equal to 78 mm. The observations reveal several key points: when the separation distance is set at 78 mm, the main lobe becomes focused at 0 degrees. However, the small curve that typically appears near -10 dB is absent. Nevertheless, the second and third lobes fit reasonably well with the expected pattern.

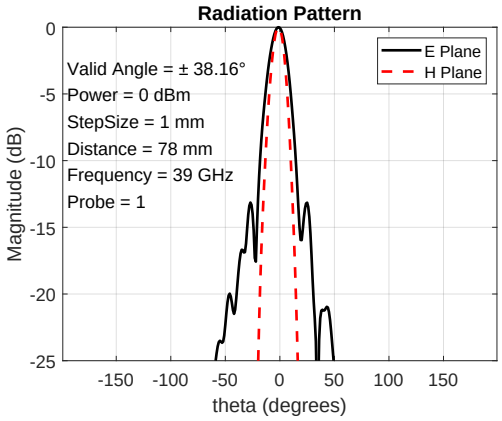

Figure 4.8: Estimated pattern for 78 mm separation distance

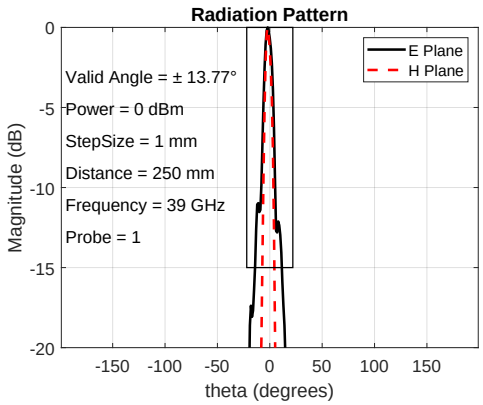

(a) Estimated Pattern

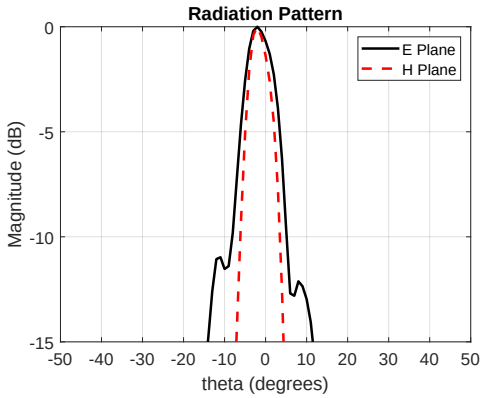

(b) Valid part of the figure 4.9a

Figure 4.9: Estimated pattern for power 0 dBm at 250 mm separation distance

In the Figure 4.9a, the estimated pattern for a separation distance of 250 mm can be observed. With an increase in distance as compared to Figure 4.8, there is a reduction in the valid angle range. To provide a clearer view of this valid region, the plot has been zoomed in and shown separately in Figure 4.9b. It's important to note that an expected small spike near -10 dB becomes evident in the plot, which fits in our expectation.

4.4 Estimated result of Active Antenna: PAAM board

The measurements of the PAAM board were conducted in another similar chamber using the same scanner mentioned in Section 3.4. Both amplitude and phase were measured using the VNA, with a separation distance of 0.55 meters between the PAAM and the probe. The measurement parameters were as follows:

- Frequency, f = 28 GHz
- Wavelength, $\lambda = \frac{c}{f} = \frac{3\times10^8}{28\times10^9} = 0.0107$ m
- DUT diameter, D = 142.7 mm
- The near-field distance was chosen as 0.55 m, calculated based on Equation 4.3 to determine the far-field distance.

The separation distance for an $N \times M$ array antenna is calculated using the following formula [26]:

$$FF \approx \frac{3}{400 f_{GHz}} \left\{ \left(2N - 1 + \frac{2}{\sqrt{\varepsilon_r}} \right)^2 + \left(2M - 1 + \frac{1}{2}\sqrt{\frac{2}{\varepsilon_r + 1}} \right)^2 \right\} \tag{4.3}$$

The actual gain of the PAAM board was reported as 52 dB at 28 GHz. After applying the NF2FF algorithm to the measurements, the gain was estimated to be 50.89 dB at 28 GHz. The reason to get such a high gain is because of the amplifier gain of the PAAM.

The radiation of the PAAM board was reported to be radiating towards 0°. However, when applying the NF2FF algorithm to the measured data, it was noticed that the estimated radiation was towards 1.6°. The possible explanations for this difference of 1.6° could be that during the measurement, the probe was bent by 0.5°, and the calibration of the center of the probe and the PAAM board had an offset of a few millimeters.

It's important to note that there is a 1.11 dB difference between the estimated gain and the actual gain. Despite compensating for the RF cable loss, several probable reasons could account for this deviation.

- Firstly, the probe compensation was not implemented for the PAAM board measurements, as it requires a specialized algorithm to be developed, which was constrained by time limitations.

- Secondly, the distance at which the measurements were conducted could be a contributing factor. Since it was a planar near-field measurement, some information may have been lost due to the limited scanning area. This limitation can potentially be overcome through spherical scanning, a concept that is elaborated on in the future work section.
- Furthermore, the alignment of the probe and the PAAM board wasn't perfectly straight, and the probe wasn't precisely centered. These factors could explain the observed deviation.

The pattern of the PAAM was not estimated. Although working with active antennas is highly intriguing, conducting the NF2FF analysis for an active antenna demands a complex setup and specialized components. Unfortunately, due to time and resource constraints, this was not feasible. Nevertheless, conducting a trial was deemed worthwhile, and the gain has been estimated.

Chapter 5
Conclusion and Future Work

5.1 Conclusion

The objective of the thesis was to develop an algorithm for predicting the far-field pattern of an antenna. To achieve this, the planar near-field measurement technique was employed to gather measurements of the DUT's radiation. The process began by calculating the distance for radiating near-field measurements, which determined the precise location for conducting the measurements. Subsequently, measurements were taken while systematically varying the input power and the separation distance between the DUT and the probe, focusing on frequencies of 28 GHz and 39 GHz.

In these measurements, the parameter of interest is the S-parameter. The algorithm follows a specific flow: first, it determines the near-electric and magnetic field strengths on the designated imaginary plane. Subsequently, it identifies the electric and magnetic surface currents. These currents are then utilized to predict the far-field radiation pattern. To put this into action, a scanning area of 164 mm $\times$ 164 mm was selected for the 28 GHz frequency, while a slightly smaller area of 163 mm $\times$ 163 mm was chosen for the 39 GHz frequency. The step sizes for these scans were set at 2 mm and 1 mm, respectively. This resulted in matrices of size 81 $\times$ 81 and 163 $\times$ 163, corresponding to the two frequencies.

- The estimated radiation pattern obtained from the proposed algorithm demonstrates a favorable resemblance to the expected radiation pattern within a reasonable range.
- However, it's important to note that some disturbances appear in the estimated radiation pattern at the 39 GHz frequency, specifically when the separation distance is less than 78 mm.
- Overall, the estimated radiation pattern at 28 GHz closely aligns with the expected pattern, whereas at 39 GHz, due to the higher frequency and correspondingly shorter wavelengths, stronger probe compensation is required.
- Both frequencies exhibit their main lobes pointing at -1 degree. This is attributed to the fact that during measurements, the DUT could not be precisely positioned flat, resulting in a tilt of approximately -1 degree.

- In regard to the estimated gain, the variation between the gain stated in the data sheet and the estimated gain falls within an acceptable range for both frequencies.

Regarding active antennas, while the pattern estimation was not performed, the gain of the PAAM was successfully estimated and falls within an acceptable range, with only a 1.11 dB difference between the estimated and expected values. Furthermore, the radiating direction was estimated with an error of only 1.6°. As part of future work, it is suggested to focus on predicting the pattern of active antennas with higher precision.

5.2 Limitations

While the proposed method successfully predicts a radiation pattern that closely aligns with the expected pattern within an acceptable range, it's important to acknowledge that there are certain limitations associated with this approach.

- Compared to cylindrical and spherical near-field measurements, planar measurements typically offer radiation pattern information within a limited angular range. However, these measurement techniques do not capture the full three-dimensional information.
- Planar near-field measurements often face constraints related to the size of the measurement plane. Furthermore, they can be time-consuming, particularly when dealing with a very large area and using smaller step sizes.
- It's important to note that the proposed measurement setup may not be accurate or suitable for active antennas where phase information becomes crucial in predicting the far-field pattern.

5.3 Future work

Despite conducting a trial to determine some far-field characteristics of the Phase Array Antenna Module (PAAM), which incorporates active elements, the results were not entirely satisfactory. Given the constraints of time and resources, a more viable solution is outlined in this section.

Understanding magnitude is relatively inexpensive compared to acquiring phase information. Therefore, a cost-efficient and optimized method for resolving phase using a Spectrum Analyzer (SA) is proposed. Obtaining magnitude information from the SA is considerably more convenient, while obtaining accurate phase information poses a more significant challenge. The setup used to measure both magnitude and phase is illustrated in Figure 5.1.

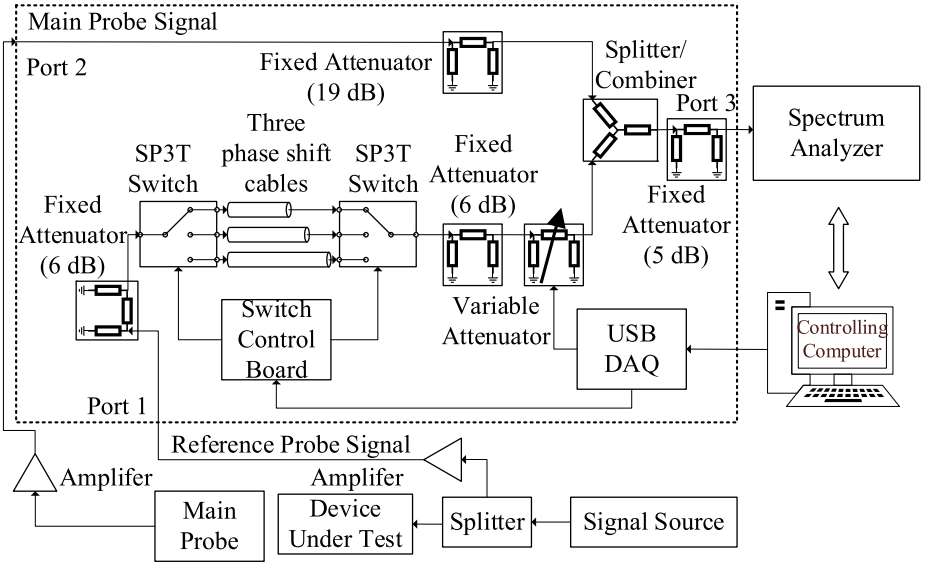

Figure 5.1: SA measurement setup block diagram [27]

In the near-field scanning technique, the primary probe signal is obtained from the scan plane of the DUT and from a fixed location on the DUT. These two signals can be considered as two input vectors, denoted as $\vec{A}$ and $\vec{B}$, with magnitudes of A and B and phases of ϕ_a and ϕ_b respectively. The resultant vector $\vec{C}$ is the sum of vectors $\vec{A}$ and $\vec{B}$. Consequently, the magnitude of $\vec{C}$ is given by equation 5.4.

$$\vec{C} = \vec{A} + \vec{B} \tag{5.1}$$

$$\vec{A} = Ae^{i\phi_a}, \vec{B} = Be^{i\phi_b} \tag{5.2}$$

$$C = \sqrt{\vec{C} \cdot \vec{C}} = \sqrt{\left(\vec{A} + \vec{B}\right) \cdot \left(\vec{A} + \vec{B}\right)} \tag{5.3}$$

$$C = \sqrt{A^2 + B^2 + 2ABcos(\phi_b - \phi_a)} \tag{5.4}$$

If the magnitudes of the two input vectors are known and similar, it becomes partially possible to determine the phase difference. Utilizing equation 5.4, the phase difference can be calculated. However, it's important to note that the sign of the phase is lost in this process, as the arc-cosine function only provides information in the range of 0° to +180°. To obtain accurate phase information with the sign, a known phase value is introduced. This can be achieved by using a switch to alter the phase-shift cable length and taking multiple measurements. The measurement process follows a specific order: first measuring the reference magnitude, followed by the probe magnitude, and then measuring the summation of the reference and probe magnitudes both with and without known phase shifts on the reference signal. If the probe magnitude is significantly smaller than the reference

magnitude, it's essential to introduce sufficient attenuation on the reference signal to ensure similar magnitudes.

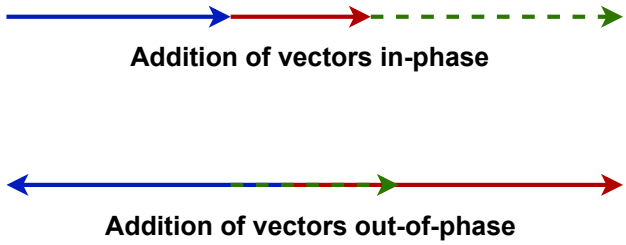

Figure 5.2: Representation of vector addition

The importance of having similar magnitude values is quite significant. When two signals are added in-phase, the maximum magnitude is achieved, whereas out-of-phase addition results in the minimum magnitude, as illustrated in Figure 5.2. As observed, if the magnitudes are similar, the difference between the maximum and minimum values is substantial. Conversely, when the magnitudes are dissimilar, this difference becomes smaller. This underscores the necessity for similarity in magnitudes because if one vector has a significantly larger magnitude than the other, it will dominate the vector summation, potentially leading to smaller uncertainties and larger errors. A more detailed explanation of this method, along with results, can be found in [27].

In addition to employing various algorithms, the careful selection of components plays a vital role in achieving accurate measurements. While a single probe that measures both electric and magnetic fields together can simplify the process and reduce complications, it's essential to choose dedicated probes for each field to potentially enhance the precision of measurements. For measuring electric field strength, electrostatic field probes are a suitable choice. They are designed specifically for this purpose. Conversely, Hall effect probes are well-suited for measuring magnetic field strength. Moreover, when it comes to assessing the far-field at a particular distance, the use of Green's dyadic function becomes valuable. Equation 5.5 provides the dyadic Green's function for the far-field, and more comprehensive information about its application can be found in reference [28].

$$\begin{aligned} \bar{G}\left(\bar{r},\bar{r'}\right) &\simeq \left[\bar{I}-\hat{r}\hat{r}\right]\frac{e^{ik\left|\bar{r}-\bar{r'}\right|}}{4\pi r} \\ &\simeq \left[\bar{I}-\hat{r}\hat{r}\right]\frac{e^{ikr}}{4\pi r}e^{-ik\hat{r}\cdot\bar{r'}} \end{aligned} \tag{5.5}$$

References

[1] Thomas A Watson. How bell invented the telephone. Proceedings of the American Institute of Electrical Engineers, 34(8):1503–1513, 1915.

[2] Rafaqat Alam Khan and Arslan Tariq. A survey on wired and wireless network. Lahore Garrison University Research Journal of Computer Science and Information Technology, 2(3):19–28, Sep. 2018.

[3] Tadao Nagatsuma, Kazutoshi Kato, and Jeffrey Hesler. Enabling technologies for real-time 50-gbit/s wireless transmission at 300 ghz. In Proceedings of the Second Annual International Conference on Nanoscale Computing and Communication, pages 1–5, 2015.

[4] Constantine A Balanis. Antenna theory: analysis and design. John Wiley & Sons, 2016.

[5] Keith Benson. Phased array beamforming IC's simplify antenna design. 53-01:1–4, Jan. 2019.

[6] Yihong Qi, Guang Yang, Lie Liu, Jun Fan, Antonio Orlandi, Hongwei Kong, Wei Yu, and Zhiping Yang. 5g over-the-air measurement challenges: Overview. IEEE Transactions on Electromagnetic Compatibility, 59(6):1661–1670, 2017.

[7] Paakinaho, L. (2022) Antenna radiation pattern - near field to far field transformation, Verkotan. Available at: `https://verkotan.com/2021/antenna-radiation-pattern-near-field-to-far-field-transformation/`

[8] Jesper E Hansen. Spherical near-field antenna measurements, volume 26. Iet, 1988.

[9] Stuart Gregson, John McCormick, and Clive Parini. Principles of planar near-field antenna measurements, volume 53. IET, 2007.

[10] Staelin, David, Ann Morgenthaler, and Jin Au Kong. Electromagnetic Waves. Upper Saddle River, NJ: Prentice Hall, 1994. ISBN: 9780132258715

[11] Phillip C Clemmow. The plane wave spectrum representation of electromagnetic fields: International series of monographs in electromagnetic waves. Elsevier, 2013.

[12] Jingnan Pan, Xu Gao, Yaojiang Zhang, and Jun Fan. Far-field radiation estimation from near-field measurements and image theory. In 2014 IEEE International Symposium on Electromagnetic Compatibility (EMC), pages 609-614, 2014.

[13] R. C. Johnson, H. A. Ecker and J. S. Hollis, "Determination of far-field antenna patterns from near-field measurements," in Proceedings of the IEEE, vol. 61, no. 12, pp. 1668-1694, Dec. 1973, doi: 10.1109/PROC.1973.9358.

[14] Brown, J. and Jull, E.V. (1961) 'The prediction of aerial radiation patterns from near-field measurements', Proceedings of the IEE Part B: Electronic and Communication Engineering, 108(42), p. 635. doi:10.1049/pi-b-2.1961.0109.

[15] D Gaetano, A Manna, F Trotta, M Bartocci, E Ciacia, V Stornelli, G Leuzzi, and L Pantoli. An active and passive antenna pattern comparison. In 2016 IEEE International Symposium on Antennas and Propagation (APSURSI), pages 2151–2152. IEEE, 2016.

[16] "IBM and Ericsson announce 5G mmWave phased array antenna module", Feb. 2017, Available: http://www.microwavejournal.com/articles/27830-ibm-and-ericsson-announce-5g-mmwave-phase-array-antenna-module

[17] Dahlman, E., Parkvall, S. and Sköld, J. (2021) 'Chapter 3, Section 3.2, Table 3.2', in 5G NR: The next generation wireless access technology. London: Elsevier, Academic Press.

[18] C. Taybi, R. K. Kwate, B. Elmagroud, A. Ziyyat and M. A. Moutaouekkil, "Probes characterization for antennas near field measurements," Proceedings of 2014 Mediterranean Microwave Symposium (MMS2014), Marrakech, Morocco, 2014, pp. 1-5, doi: 10.1109/MMS.2014.7088986.

[19] Bofei Wang. Near-field measurement system for 5g advanced antenna system at mm-wavelength, 2020. LUP Student Paper.

[20] Aperture antenna (2023) Wikipedia. Available at: https://en.wikipedia.org/wiki/Aperture_(antenna)

[21] Gustafsson, M. (2021) 'ETEN10 - Antenna Technology'. canvas.education.lu.se/courses.

[22] S. J. Orfanidis, "Electromagnetic Waves and Antennas", 2016. Available at: https://www.ece.rutgers.edu/~orfanidi/ewa/

[23] A. Yaghjian, "An overview of near-field antenna measurements," in IEEE Transactions on Antennas and Propagation, vol. 34, no. 1, pp. 30-45, January 1986, doi: 10.1109/TAP.1986.1143727.

[24] Constantine A Balanis. Modern antenna handbook. John Wiley & Sons, 2011.

[25] K Van Caekenberghe and J Logan. Nf2ff. MATLAB Central File Exchange, 2023.

[26] W. E. HAJJ, T. Andriamiharivolamena, J. A. Del Real and N. Asrih, "Definition of Far Field Measurement Distance for 5G mmW Antenna Arrays: Application on N × M Patch Arrays," 2022 16th European Conference on Antennas and Propagation (EuCAP), Madrid, Spain, 2022, pp. 1-4, doi: 10.23919/EuCAP53622.2022.9769345.

[27] S. Marathe et al., "Spectrum Analyzer-Based Phase Measurement for Near-Field EMI Scanning," in IEEE Transactions on Electromagnetic Compatibility, vol. 62, no. 3, pp. 848-858, June 2020, doi: 10.1109/TEMC.2019.2920344.

[28] K Sarabandi. Dyadic green's function. Theory of Wave Scattering from Rough Surfaces and Random Media, 2009.

Appendix A

Some extra material

The appendix section provides additional plots that depict variations in distance and power between the Device Under Test (DUT) and the Open-Ended Rectangular Waveguide (OERWG). All the plots in the appendix were generated using the same Near-field to Far-field (NF2FF) algorithm implemented during the thesis, and the measurements were conducted with the same setup.

A.1 Results for 28 GHz

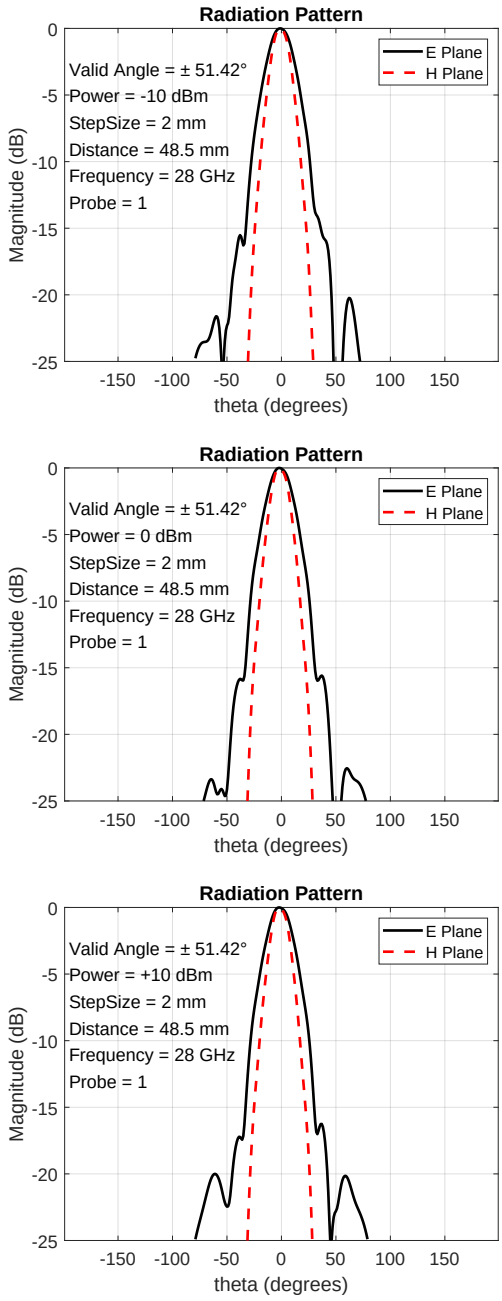

Figure A.1: Estimated results at separation distance 48.5 mm

A.2 Results for 28 GHz

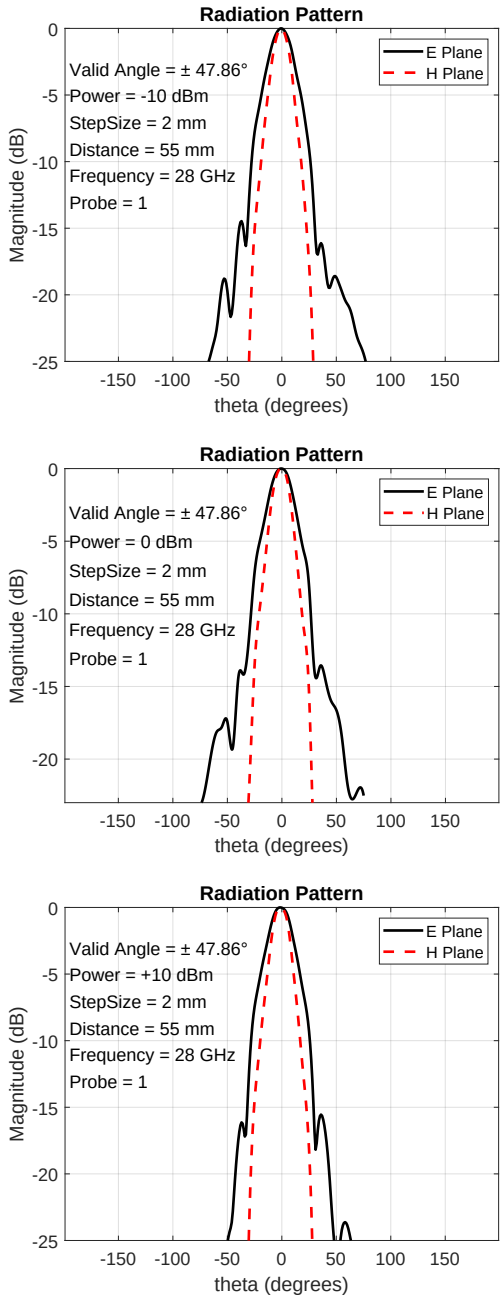

Figure A.2: Estimated results at separation distance 55 mm

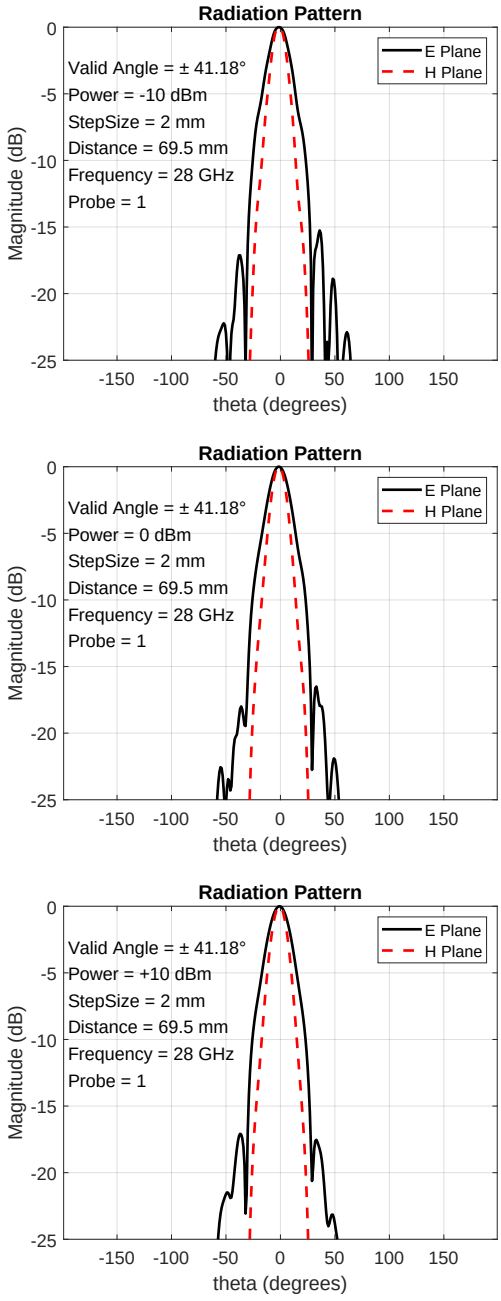

Figure A.3: Estimated results at separation distance 69.5 mm

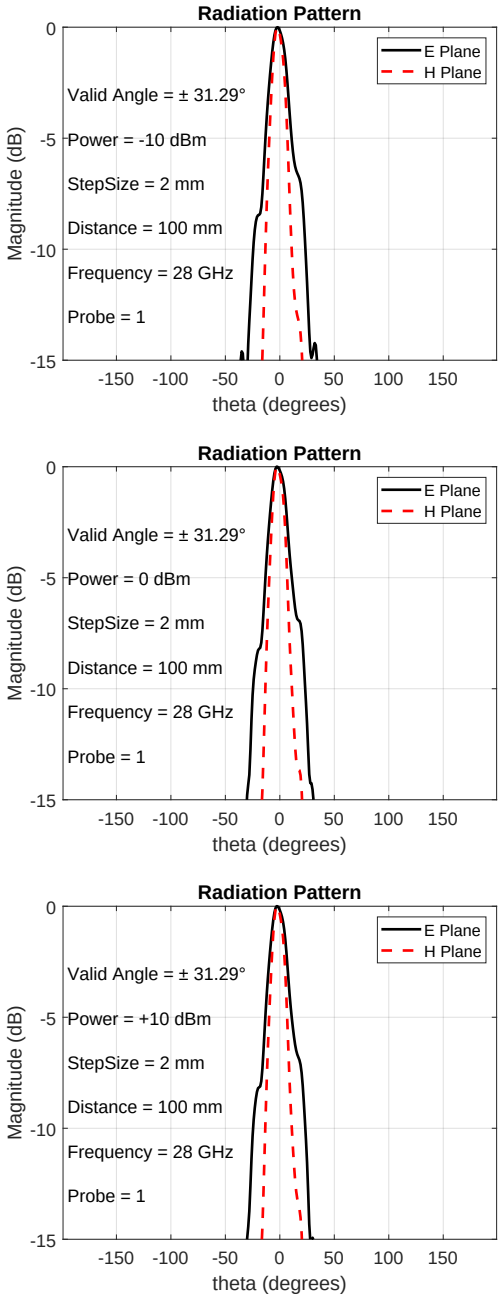

Figure A.4: Estimated results at separation distance 100 mm

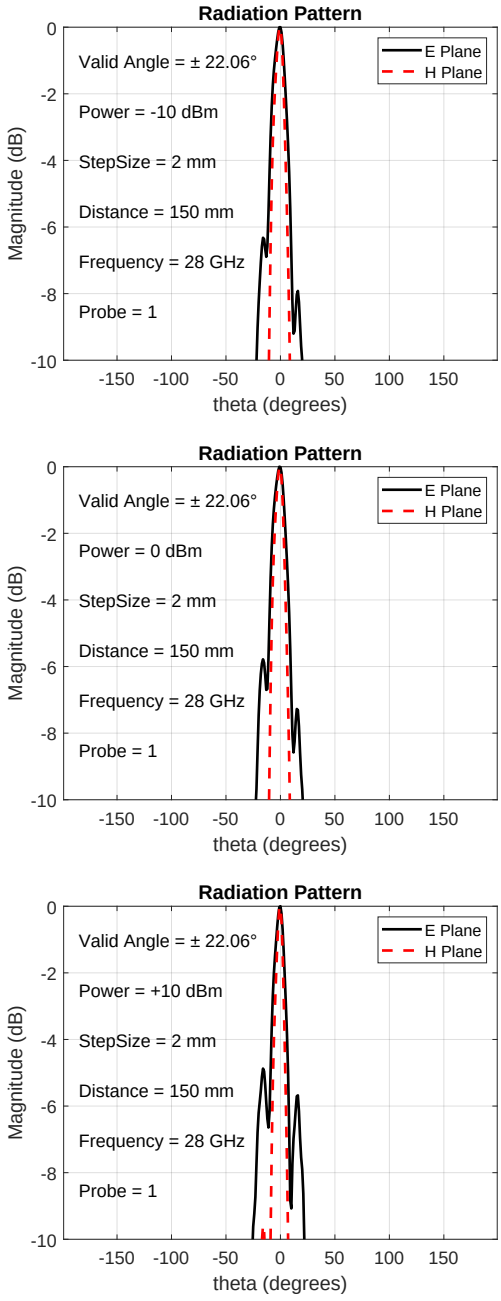

Figure A.5: Estimated results at separation distance 150 mm

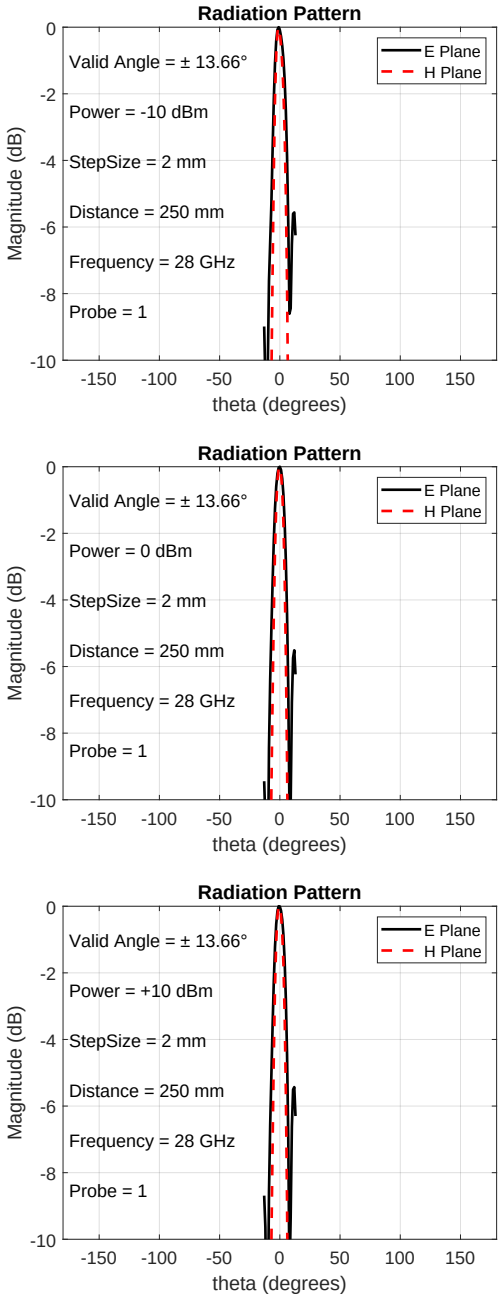

Figure A.6: Estimated results at separation distance 250 mm

A.3 Results for 39 GHz

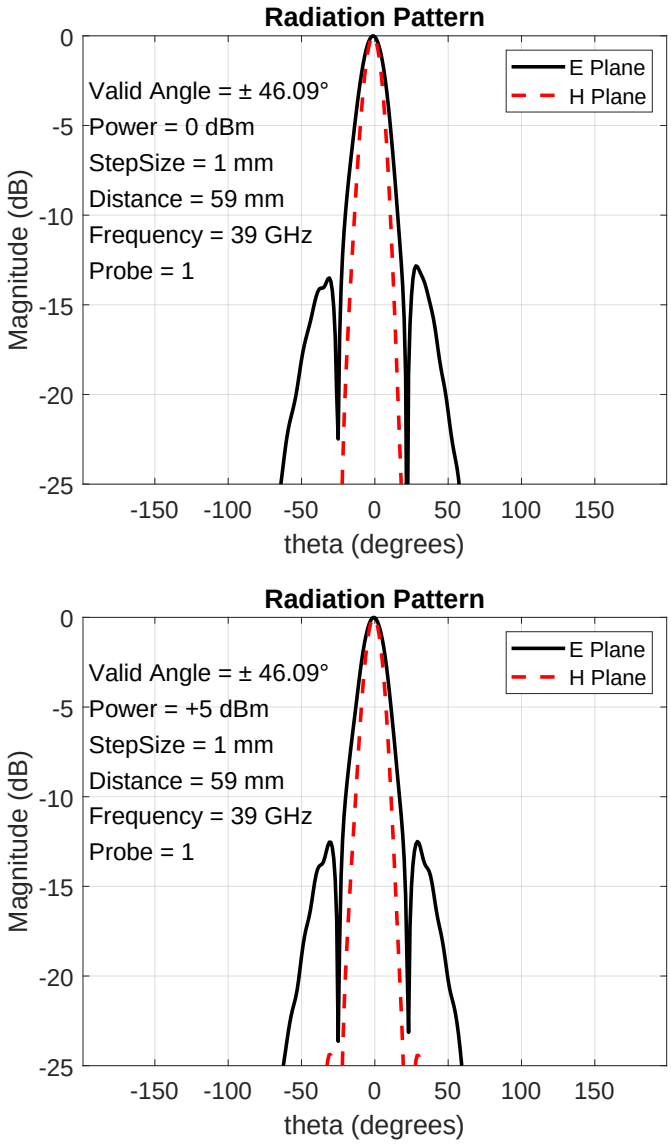

Figure A.7: Estimated results at separation distance 59 mm

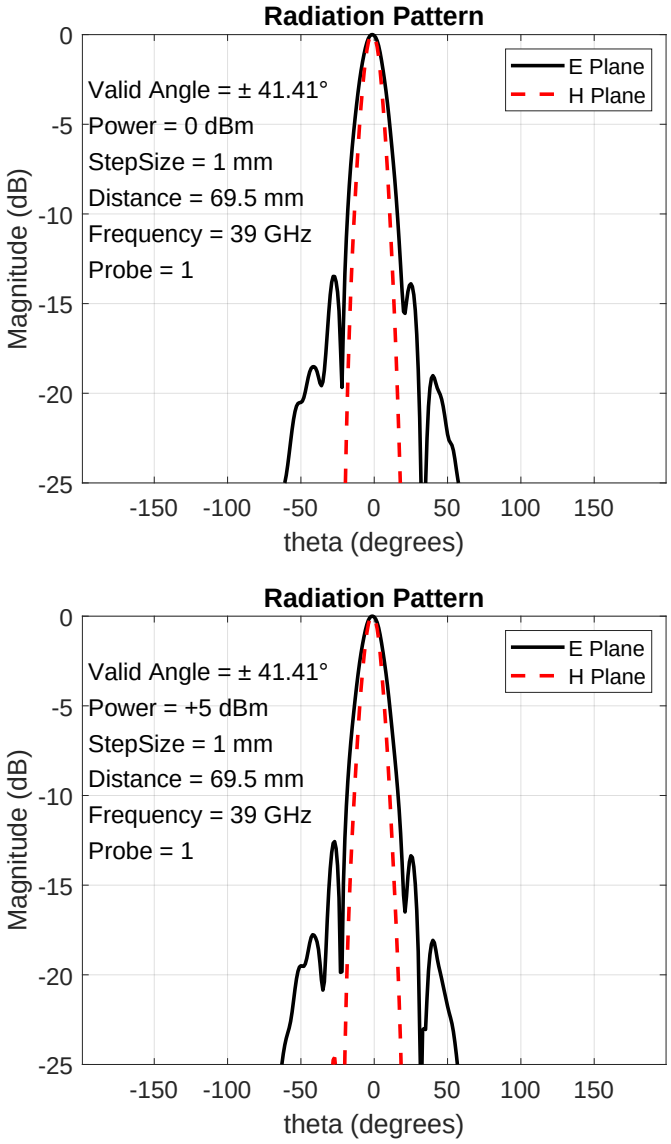

Figure A.8: Estimated results at separation distance 69.5 mm

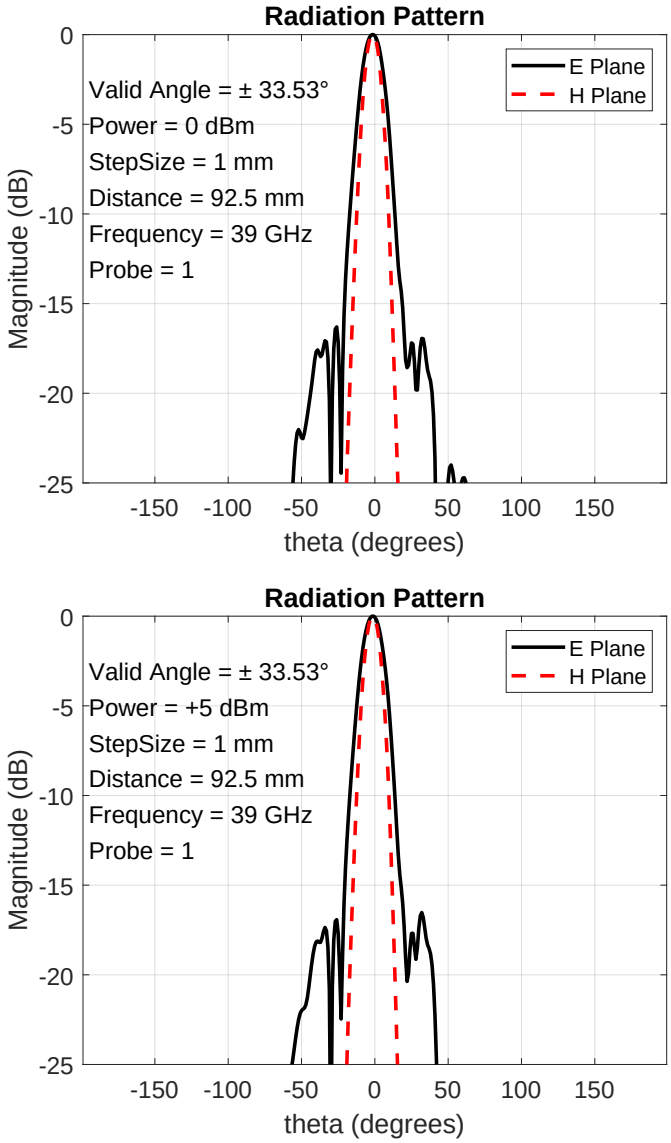

Figure A.9: Estimated results at separation distance 92.5 mm

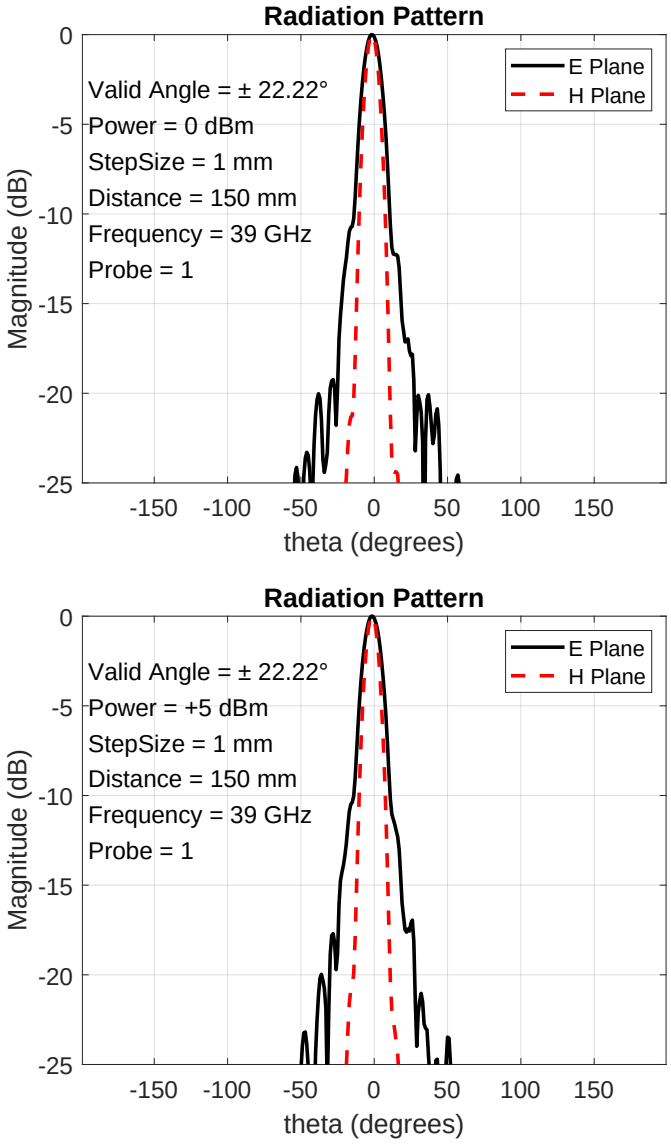

Figure A.10: Estimated results at separation distance 150 mm